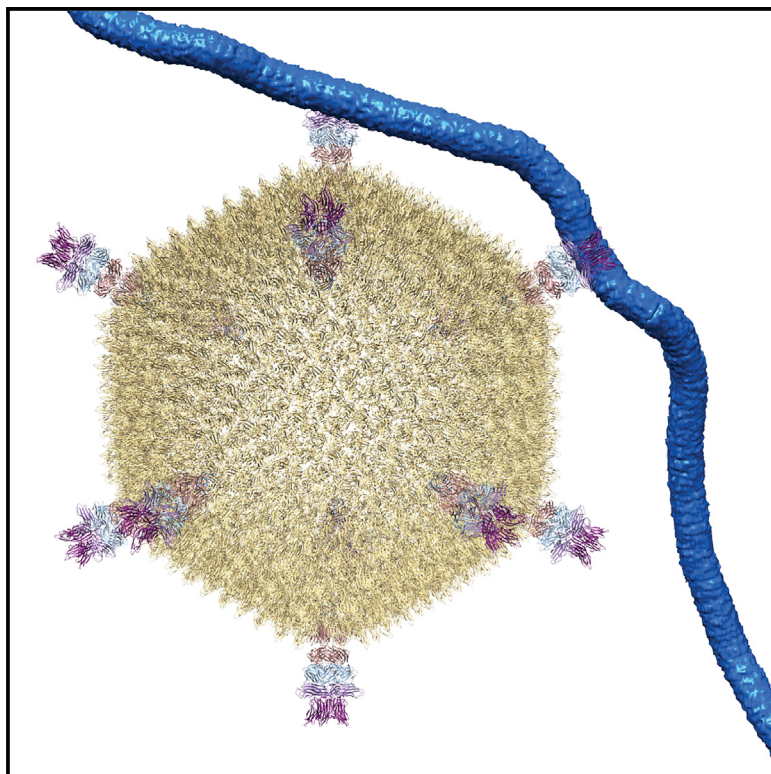


# Structure

## The Molecular Mechanism of Cellular Attachment for an Archaeal Virus

### Graphical Abstract



### Authors

Ross Hartman, Brian J. Eilers,  
Daniel Bollschweiler,  
Jacob H. Munson-McGee,  
Harald Engelhardt, Mark J. Young,  
C. Martin Lawrence

### Correspondence

myoung@montana.edu (M.J.Y.),  
lawrence@montana.edu (C.M.L.)

### In Brief

Viral attachment and entry in the archaeal domain of life are poorly understood. Hartmann et al. show that STIV, a model archaeal virus, uses turret proteins to recognize pili-like host structures, and they provide a molecular model for initial viral attachment. A substantial cell surface glycan shield is also identified.

### Highlights

- The crystal structure of STIV C381 reveals a triple jelly roll fold
- Cryo-EM shows a thick (>30 nm) glycan layer shielding the *S. solfataricus* S-layer
- Cryoelectron tomography yields pseudo-atomic models for virus host interactions
- C381 binds host cell pili utilizing conserved residues in the second and third domains

# The Molecular Mechanism of Cellular Attachment for an Archaeal Virus

Ross Hartman,<sup>1,6</sup> Brian J. Eilers,<sup>1,6</sup> Daniel Bollscheieler,<sup>2</sup> Jacob H. Munson-McGee,<sup>3</sup> Harald Engelhardt,<sup>2</sup> Mark J. Young,<sup>3,4,5,\*</sup> and C. Martin Lawrence<sup>1,5,7,\*</sup>

<sup>1</sup>Department of Chemistry and Biochemistry, Montana State University, Bozeman, MT 59717, USA

<sup>2</sup>Department of Molecular Structural Biology, Max-Planck-Institute for Biochemistry, Martinsried, Germany

<sup>3</sup>Department of Microbiology and Immunology, Montana State University, Bozeman, MT 59717, USA

<sup>4</sup>Department of Plant Sciences and Plant Pathology, Montana State University, Bozeman, MT 59717, USA

<sup>5</sup>The Thermal Biology Institute, Montana State University, Bozeman, MT 59717, USA

<sup>6</sup>These authors contributed equally

<sup>7</sup>Lead Contact

\*Correspondence: myoung@montana.edu (M.J.Y.), lawrence@montana.edu (C.M.L.)

<https://doi.org/10.1016/j.str.2019.09.005>

## SUMMARY

*Sulfolobus* turreted icosahedral virus (STIV) is a model archaeal virus and member of the PRD1-adenovirus lineage. Although STIV employs pyramidal lysis structures to exit the host, knowledge of the viral entry process is lacking. We therefore initiated studies on STIV attachment and entry. Negative stain and cryoelectron micrographs showed virion attachment to pili-like structures emanating from the *Sulfolobus* host. Tomographic reconstruction and sub-tomogram averaging revealed pili recognition by the STIV C381 turret protein. Specifically, the triple jelly roll structure of C381 determined by X-ray crystallography shows that pilus recognition is mediated by conserved surface residues in the second and third domains. In addition, the STIV petal protein (C557), when present, occludes the pili binding site, suggesting that it functions as a maturation protein. Combined, these results demonstrate a role for the namesake STIV turrets in initial cellular attachment and provide the first molecular model for viral attachment in the archaeal domain of life.

## INTRODUCTION

Once thought to occur only in extreme environments, Archaea are now estimated to constitute 20% of the total biomass on Earth (DeLong and Pace, 2001). In oceans, for example, Archaea constitute 30% of prokaryotic diversity in the pelagic zone, where members of the Crenarchaeota and Thaumarchaeota represent the oceans most abundant phyla (Karner et al., 2001; Pina et al., 2011). Furthermore, more than 80% of the biomass in marine subsurface sediments is also archaeal (Lipp et al., 2008). Thus, it is not surprising that Archaea play significant roles in global nitrogen and carbon cycles (Adam et al., 2017; Falkowski et al., 2008), including a predominant role in ammonia oxidation in soils (Leininger et al., 2006; Wuchter et al., 2006) and an

exclusive role in methanogenesis (Thauer et al., 2008), which is thought to be a strictly archaeal metabolism. In addition, Archaea are also an important, although poorly understood component of the human microbiome (Adam et al., 2017; Lloyd-Price et al., 2016). For these reasons, there is now significant interest in Archaea, and by extension, archaeal viruses (Lawrence et al., 2009; Pina et al., 2011).

*Sulfolobus* turreted icosahedral virus (STIV-1) is among the best studied archaeal viruses, where it serves as a model system for viruses in this third domain of life (Brumfield et al., 2009; Dellas et al., 2015; Fu and Johnson, 2012; Fu et al., 2010; Fulton et al., 2009; Khayat et al., 2005, 2010; Larson et al., 2006, 2007; Maaty et al., 2006, 2012; Ortmann et al., 2008; Rice et al., 2004; Snyder et al., 2011, 2013a, 2013b; Veesler et al., 2013; Wirth et al., 2011). STIV-1 packages a 17.5-kbp circular double-stranded DNA genome, encoding 37 open reading frames, within a 75-MDa icosahedral shell built upon a pseudo T = 31d icosahedral lattice (Matty et al., 2006; Rice et al., 2004), with an internal lipid envelope present between the nucleic acid core and the outer protein shell. The major capsid protein adopts the double jelly roll fold, which places STIV within the adenovirus-PRD1 viral lineage, and suggests the possibility that these viruses derive from a common ancestor existing more than 3 billion years ago, before the divergence of Bacteria, Archaea, and Eukarya (Khayat et al., 2005; Rice et al., 2004; Veesler et al., 2013).

Its namesake turret-like assemblies are present at the 5-fold vertices. Pentameric assemblies composed of three viral proteins, A55, A223, and C381, constitute each turret (Khayat et al., 2010; Matty et al., 2006; Veesler et al., 2013). A223 adopts a non-canonical double jelly roll fold and positions the N-terminal jelly roll domain within the capsid shell at the penton base. N-terminal extensions on the A223 pentamer project into the capsid, where they interdigitate with the C-terminal end of the A55 pentamer to form a ten-stranded, hemolysin-like, antiparallel  $\beta$  barrel, with the N terminus of A55 firmly anchored in the internal lipid layer (Veesler et al., 2013). In contrast, the A223 C-terminal jelly roll domain projects outward from the exterior surface of the capsid where it interacts with C381 to collectively form the exterior turret complex, which protrudes 13 nm above the capsid surface (Veesler et al., 2013). At times a fourth protein, thought to be

**Table 1. Data Collection**

Dataset	Se Peak	Native
Wavelength (Å)	0.97893	0.95369
Space group	P1	P1
Cell constants		
a, b, c (Å)	82.39, 166.95, 187.00	81.77, 167.00, 186.98
α, β, γ (°)	81.83, 82.16, 81.20	81.84, 82.17, 81.44
Resolution range <sup>a</sup> (Å)	40–3.2 (3.26–3.2)	39.2–1.76 (1.86–1.76)
Unique reflections <sup>a</sup>	158,776	837,015
Average redundancy <sup>a</sup>	3.8(3.5)	3.6(3.4)
I/σ <sup>a</sup>	56(24.7)	58.3(6.5)
Completeness (%)	98.5(96.3)	90.9(63.9)
R <sub>sym</sub> <sup>a,b</sup> (%)	11.2 (36.7)	4.3 (35.4)

<sup>a</sup>Numbers in parentheses refer to the highest-resolution shell.

<sup>b</sup>R<sub>sym</sub> = 100 \* Σ<sub>h</sub>Σ<sub>i</sub>|I<sub>i</sub>(h) - <|I(h)>/ Σ<sub>h</sub>|I<sub>i</sub>(h)|, where I<sub>i</sub>(h) is the ith measurement of reflection h and <|I(h)> is the average value of the reflection intensity.

C557, is also present as “petals” that decorate the STIV turrets (Khayat et al., 2010; Maaty et al., 2006; Rice et al., 2004). The function of C557 remains an enigma (Fulton et al., 2009; Rice et al., 2004). Interestingly, in STIV-2 the A223 and C381 homologs are present as a fusion into a single turret protein (Happonen et al., 2010).

Whole-cell cryoelectron tomography (CET) identified mature virions, procapsids without genome cores, and partially assembled particles in the cytoplasm of the infected *Sulfolobus* host (Fu et al., 2010). This suggests the capsid and inner membrane of STIV-1 co-assemble in the cytoplasm to form a procapsid, which is then packaged with DNA (Fu et al., 2010), presumably through a unique vertex that includes B204, the presumptive packaging ATPase (Dellas et al., 2015). This assembly model also requires that the lipids constituting the viral membrane are recruited directly in the cytoplasm, rather than by a budding mechanism from the host membrane during virion release.

Following assembly, STIV-1 then uses a remarkable, seven-sided pyramid-like structure formed by a single viral protein (C92) to lyse the cell (Brumfield et al., 2009; Snyder et al., 2011). The base of this seven-sided pyramid is embedded within the cyclic tetra-ether lipid membrane of the host cell and extends 20–150 nm above the extracellular proteinaceous surface layer (S-layer). During lysis, the seven leaflets of the pyramid open, producing ~100-nm holes through which the newly formed virus particles exit the cell (Brumfield et al., 2009; Fu et al., 2010; Snyder et al., 2011, 2013a, 2013b).

In contrast to assembly, genome packaging, and release, our understanding of STIV attachment and entry is limited, and speculative (Happonen et al., 2010; Khayat et al., 2010; Rice et al., 2004; Veesler et al., 2013). For this reason, we undertook studies on the initial attachment of STIV to *S. solfataricus* and show here that initial attachment is to host pili. Using the previously determined structure of STIV-1 by high-resolution cryoelectron microscopy (cryo-EM) (Veesler et al., 2013), a high-resolution crystallographic structure of C381 described here, and CET with subtomographic averaging, the interaction is localized to

conserved residues lining a cleft formed by the second and third jelly roll domains of C381.

The crystal structure of C381 was briefly described in the context of a cryo-EM single-particle analysis of STIV in which the turrets were not well resolved, and its coordinates were included in the deposition to complete the atomic model of the full virus. However, the structural analysis was minimal, and limited to discussion of its overall triple jelly roll architecture (Veesler et al., 2013). Here we begin by reporting the detailed structural analysis of C381.

## RESULTS

### The C381 Crystal Structure

N-terminal His-tagged C381 was expressed in *E. coli* and purified using immobilized metal affinity and size-exclusion chromatography. Similar to other capsid proteins from thermophilic archaeal viruses amenable to crystallographic study (Goulet et al., 2010; Hochstein et al., 2015, 2018; Khayat et al., 2005; Szymczyna et al., 2009; Veesler et al., 2013), the purified protein eluted as a monomer. However, C381 crystallized in space group P1 with four pentameric assemblies in the asymmetric unit/unit cell ( $Z = 20$ , 834 kDa). The initial structure was determined at 3.2 Å resolution using Se-Met-incorporated C381, single-wavelength anomalous diffraction at the Se peak, and non-crystallographic symmetry averaging. Phases were then transferred to a high-resolution native dataset and extended to 1.9 Å (Tables 1 and 2).

Within the context of the viral turret, the N-terminal jelly roll domain of C381 is closest to the capsid surface, interacting with the C-terminal domain of A223, which forms the penton base in the STIV capsid. In contrast, the C-terminal jelly roll is distant from the capsid surface, and is present at the tips of the turrets, with the second jelly roll domain intermediate between the N- and C-terminal jelly roll domains (Figure 1).

The canonical viral capsid jelly roll fold is a β sandwich, with two four-stranded antiparallel β sheets juxtaposed against each other (Harrison et al., 1978; Richardson, 1981; Rossmann et al., 1983). Historically, the first β sheet is composed of strands B, I, D and G (BIDG), and the second of strands C, H, E, and F (CHEF) (Harrison et al., 1978; Rossmann et al., 1983). Relative to this canonical fold, the second and third domains of C381 are largely devoid of additional secondary structural elements (Figure 1), although a two-residue β bulge is present in strand B of the second domain (B<sub>2</sub>), giving the appearance of a bipartite strand that is analogous to the bipartite strand B in domain 1 of the STIV coat protein (Khayat et al., 2005).

In contrast, the first jelly roll domain houses additional secondary structural elements. An N-terminal β strand (B1) precedes strand B<sub>1</sub>, and an α helix (α1) and three successive β strands (β2, β3, and β4) are inserted between stands B<sub>1</sub> and C<sub>1</sub>. Strands β3 and β4 form an extended two-stranded antiparallel β finger. The short β2 strand runs antiparallel to β strand C<sub>1</sub> along the outside edge of the C<sub>1</sub>H<sub>1</sub>E<sub>1</sub>F<sub>1</sub> sheet. Similarly, the C terminus of β4 briefly runs antiparallel to the N-terminal end of B<sub>1</sub>. Collectively, these N-terminal embellishments facilitate interactions with the C-terminal domain of A223, present at the penton base (Veesler et al., 2013), and augment the inter-subunit domain1-domain1 contacts within the C381 pentamer (Figure 1),

**Table 2. Model Refinement**

R <sub>work</sub> <sup>a</sup> (%)	18.8 (34.9)
R <sub>free</sub> <sup>a</sup> (%)	21.7 (37.2)
Real space CC <sup>b</sup> (%)	86.9
Mean B value, overall (Å <sup>2</sup> )	29.3
Coordinate error (based on maximum likelihood) (Å)	0.26
RMSD from ideality	
Bonds (Å)	0.009
Angles (°)	1.180
Ramachandran plot (%) <sup>c</sup>	
Most favored	96.8
Additional allowed	3.2
PDB	PDB: 4IND

<sup>a</sup>R<sub>work</sub> =  $\sum ||F_o - F_c|| / \sum F_o$ , where F<sub>o</sub> and F<sub>c</sub> are the observed and calculated structure factor amplitudes used in refinement. R<sub>free</sub> is calculated as R<sub>work</sub>, but using the "test" set of structure factor amplitudes that were withheld from refinement (4.9%).

<sup>b</sup>Correlation coefficient (CC) is agreement between the model and 2mF<sub>o</sub> – DF<sub>c</sub> electron density map.

<sup>c</sup>Calculated using MolProbity (Davis et al., 2007).

where strand β3 in the β finger runs antiparallel to β1 in the neighboring subunit, to form an inter-subunit three-stranded antiparallel β sheet.

Within a single subunit, the first two jelly roll domains are oriented with the CD, EF, and GH loops projecting in toward the 5-fold axis, and the BC, DE, FG and HI loops facing outward. Overall, the relative orientation of the two domains with respect to each other is similar to that in the major capsid proteins for STIV, PRD-1 and adenovirus. In these classic double jelly roll folds, the BC, DE, FG and HI loops all face the exterior surface. In addition, the two domains are aligned parallel to each other, and include a few H-bond interactions between strand F of the first domain and strand B of the second domain. Thus, the two-domain fold can be visualized as a central, eight-stranded β sheet (CHEFB'IDG') that is flanked on each face by the four-stranded BIDG and C'H'E'F sheets, respectively. Indeed, the arrangement is similar in C381; however, the β bulge present in strand B<sub>2</sub> of the second domain results in an antiparallel rather than parallel interaction between strands F<sub>1</sub> and B<sub>2</sub> (Figures 1 and S1).

In contrast, the third domain is rotated 90° relative to domain 2. But, like the preceding domains its B<sub>3</sub>C<sub>3</sub>, D<sub>3</sub>E<sub>3</sub>, F<sub>3</sub>G<sub>3</sub> and H<sub>3</sub>I<sub>3</sub> loops are solvent exposed, projecting up and outward at the tips of the turret, while the three loops at the opposite end of the sandwich (C<sub>3</sub>D<sub>3</sub>, E<sub>3</sub>F<sub>3</sub> and G<sub>3</sub>H<sub>3</sub>) pack against the exposed edges of strands G<sub>2</sub> and H<sub>2</sub> (Figure 1).

The C5 rotational symmetry of the pentamer results in three pentameric rings composed of domains 1, 2 and 3, respectively. Within the pentameric domain 3 assembly, we were fascinated to find that adjacent subunits recapitulate the inter-jelly roll interactions described above for the STIV, PRD-1 and adenovirus MCPs; specifically, the F<sub>3</sub> strand in each subunit runs antiparallel to the B<sub>3</sub> strand of the adjacent subunit, resulting in an eight-stranded inter-subunit β sheet that spans each subunit interface (Figures 1 and S1). Overall, the organizational similarity of domains 1 and 2 to the classic double jelly roll MCPs in STIV,

PRD-1 and adenovirus suggest that the first two domains of C381 may have evolved from a double jelly roll MCP. Similarly, the conserved inter-subunit interactions of the third domain may suggest that, while a subsequent addition, it too is derived from a double jelly roll capsid protein.

### Structural Similarity

Each of the individual domains was submitted for a DALI search to identify structural similarity with other proteins (Holm and Rosenstrom, 2010). Domain 1 shows greatest similarity to the carbohydrate binding module of endo-1,4-β-xylanase and the ligand binding domains of other hydrolases (PDB: 2WYS) (Z = 9.2) (Najmudin et al., 2010). In this non-catalytic carbohydrate binding domain, a polysaccharide binding groove runs across the solvent-exposed face of the CHEF sheet, perpendicular to the direction of the β strands (Figure S2). When superimposed on the C381 pentamer, this "carbohydrate binding groove" is occupied by the β finger of a neighboring C381 subunit. The structural equivalent of the carbohydrate binding groove in C381 domain 1 is thus used in constructing the C381 pentamer, where it is an important element of the subunit interface (Figure 2).

In contrast, domains 2 and 3 are most similar to other viral proteins. For domain 2 greatest similarity is found to the knob domain of the tail needle tip in podovirus HS1 (Figure S2) (PDB 4K6B) (Z = 8.5) (Leavitt et al., 2013). Like other Podoviridae, this phage has a long thin shaft for a tail needle that serves as a DNA exit channel plug. The knob domain is also distal to the viral capsid, in a position that would allow first contact with the outer bacterial membrane during adsorption. However, genetic alteration of the knob domain does not affect host specificity (presumably controlled by the six tail-spike proteins) and instead suggests a role in controlling DNA ejection into the host. Still, P22-like knob domains are structurally similar to the fiber knobs of bacteriophage PRD1 and adenovirus, which do mediate primary cell attachment (Leavitt et al., 2013; Wu and Nemerow, 2004). Overall, then, these structural similarities suggest potential roles for C381 domain 2 in viral attachment and/or genome release.

Greatest structural similarity to domain 3 is found with the protrusion or "P" domain of the infectious bursal disease virus (IBDV) VP2 subviral particle (Figure S2) (PDB: 2DF7) (Z = 8.2) (Lee et al., 2006). The P domain of IBDV VP2, also presumed to be involved in interaction with cellular receptors (Lee et al., 2006), is rotated by 90° relative to the shell or "S" domain of VP2, and sits end-on atop the S domain jelly roll fold, utilizing its CD, EF, and GH loops to mediate the interaction. In this context, the S and P domains of the IBDV VP2 trimer appear analogous to the second and third domains of the C381 pentamer, again suggesting a role for C381 in viral attachment.

### Conserved Residues

To identify C381 residues serving conserved functions, we queried available hot spring metagenomes and genomic data for relevant archaeal organisms and viruses with STIV C381 and its homolog from STIV-2 (Happonen et al., 2010). The search returned a total of 65 C381-like sequences. Sequences at 75% full length or greater were used to construct a phylogenetic tree that showed the presence of three distinct clades,

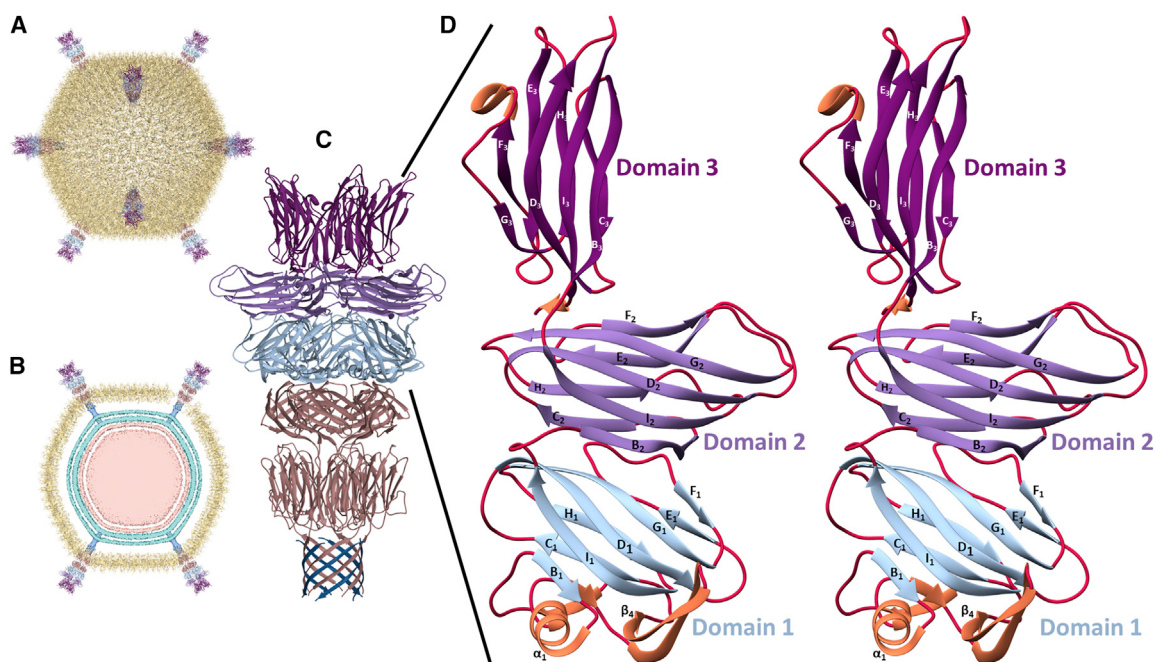


**Figure 1. Structure of STIV C381**

(A) The composite STIV1 atomic structure. The major coat protein, which exhibits a double jelly roll fold and forms a pseudo  $T = 31L$  lattice is in wheat, while proteins composing the turret are various shades of blue and purple.

(B) A cross-section through the atomic model and internal structure from single-particle analysis reveal the internal lipid membrane in light blue, and density for the double-stranded DNA genome (pink). Basement layers of the turret structure are anchored in the internal membrane.

(C) The structure of a single turret.  $\beta$  strands emanating from the A55 membrane anchor are at the bottom in blue where they interdigitate with the N terminus of A223 to form a ten-stranded hemolysin-like  $\beta$  barrel. The two-domain structure of A223 is shown above that in pink, followed by the three-domain structure of C381 in light blue, light purple, and dark purple at the top.

(D) Stereo pair of the C381 subunit with the BIDG and CHEF sheets of each domain labeled. The BIDG sheets face the viewer, while the CHEF sheets are away from the viewer. This results in solvent-exposed BC, DE, FG, and HI loops, while the CD, EF, and GH loops in domains 2 and 3 face the turret axis, and for domain 3 are at the interface with domain 2. Domains 2 and 3 are minimal jelly roll folds, while domain 1 harbors embellishments involved in subunit interactions. See also Figure S1.

representing sequences more closely related to STIV-1, those more closely related to STIV-2, and a third clade distinct from either of these (Figure S3). Intriguingly, sequences belonging to both the STIV-1 and STIV-2 clades were found to coexist in the same thermal feature. A multiple sequence alignment with all sequences from each of the three clades revealed a paucity of strictly conserved residues. However, when the alignment was confined to the 55 STIV-1-like sequences from clade 1, 143 of the 381 residues (37.5%) were strictly conserved (Figure S4).

### The C381 Subunit Interface

As expected, most of the strictly conserved side chains are buried within the hydrophobic cores of the jelly roll domains, presumably serving a largely structural role. However, 54 strictly conserved residues were found at the subunit interfaces. Of these, 12 were positively charged (nine Lys and three Arg), 16 were polar (five Tyr, four Asn, four Gly, two Thr, and one Ser), and 16 negatively charged (ten Glu and six Asp), at least at the intracellular pH of *Sulfolobus* (pH 6.5) at which STIV-1 assembles (Fu et al., 2010; Moll and Schäfer, 1988). Only nine were hydrophobic (two Pro, two Trp, one Ala, one Phe, one Val, one Leu, and one Ile).

In this context, the total surface area per subunit is  $\sim 17,000 \text{ \AA}^2$  with  $\sim 2,400 \text{ \AA}^2$  buried at each of the two contact surfaces, giving

a total buried surface area of  $4,800 \text{ \AA}^2$  (38%) per subunit. Consistent with the large buried surface area, PISA (Krissinel and Henrick, 2007) gives a complex formation significance score of 0.994. PISA also identifies 46 H-bond and 20 salt bridge interactions at each of the interacting surfaces, again indicating the hydrophilic nature of the interface. The subunit interface surfaces of the first and second domains are largely devoid of conserved hydrophobic side chains, leaving six of nine conserved hydrophobics at the domain 3/domain 3 interface. These residues form a small hydrophobic interface between strictly conserved Val330, Trp331, Ala335, Pro341, and Trp344 on one subunit with strictly conserved Phe271 (and conserved hydrophobics at 370 and 372) on the neighboring subunit. Notably, Phe271, Val330, and Trp331 lie within strands F<sub>3</sub> and B<sub>3</sub> at the inter-strand interface between adjacent subunits (Figure S1B).

### The A223 Interface

In contrast to the subunit interfaces within the C381 pentamer, the C381 interface with A223 shows only four strictly conserved residues (domain 1: Asn33, Tyr40, Leu42, and Thr89), and thus is not well conserved. However, like the inter-subunit C381 interface, it is largely hydrophilic in nature. Overall, the hydrophilic C381 subunit interfaces and corresponding lack of solvent-exposed hydrophobic residues likely plays an important

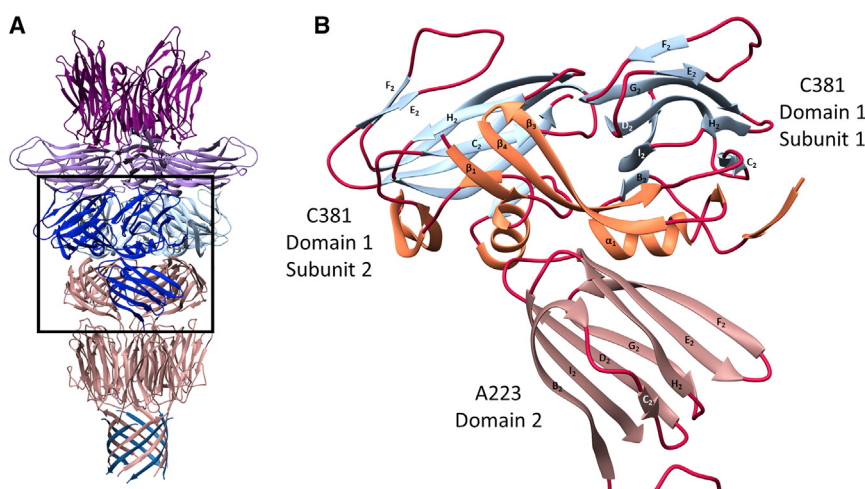


**Figure 2. C381 Domain 1 Interactions**

(A) Structure of the pentameric STIV turret with specific C381 domain 1 inter-subunit interactions highlighted in dark blue (black box).  
(B) Enlargement of the three highlighted domains in the boxed region of (A). The  $\beta_3/\beta_4$  finger of C381 domain 1 subunit 1 packs across a shallow groove of the domain 1 CHEF sheet in the adjacent (second) subunit.  $\beta_4$  runs parallel to  $\beta_1$  of the adjacent subunit to give a mixed three-stranded  $\beta$  sheet at the subunit interface while helix  $\alpha_1$  of C381 interacts with strands  $E_2$  and  $F_2$  (pink) of A223 (a double jelly roll) to anchor the C381 pentamer to the A223 penton base.

See also Figure S2.

role in stabilizing the monomeric form of the recombinant protein.

### The Petal Interface

A prominent feature of the initial 27-Å resolution single-particle reconstruction of STIV (EMDB: EMD-20618) are the petal-like decorations on the viral turrets (Rice et al., 2004). The only capsid protein with a molecular weight near the predicted 63 kDa mass of these decorations is C557 at 59.4 kDa (Khayat et al., 2010; Maaty et al., 2006). Later reconstructions showed either absence or partial occupancy of the petals at each turret, inhibiting further structural analysis of the petals (Khayat et al., 2010; Veesler et al., 2013). To identify interactions between C381 and the petals, a difference map was calculated by subtracting the more recent high-resolution reconstruction from the earlier 27-Å reconstruction. The difference map indicates the petals recognize the first and second jelly roll domains within a single C381 subunit (Figure 3). Specifically, petal density intersects the  $B_1C_1$  and  $D_2E_2$  loops of C381. The interaction appears to be mediated by non-conserved hydrophilic residues, although some conserved residues present in the vicinity may also serve as contacts. These include the aromatics Y186, F/Y194, and Y/F245, in addition to the polar N188 residue. Given the small contact surface area between C381 and the petals, it is not surprising that these structures are lost during virion purification or shed as a result of virus maturation.

### Virion Adsorption Kinetics and Virus Half-Life

We previously suggested that the STIV turrets are involved in host cell recognition and attachment (Khayat et al., 2010). The structural similarity of C381 domains 2 and 3 to proteins involved in host cell attachment and genome release, such as HS1 and Sf6 of the P22-like phage (Bhardwaj et al., 2011; Leavitt et al., 2013) and VP2 of IBDV (Lee et al., 2006), as well as the role of the knob-like proteins of adenovirus (Bergelson et al., 1997; Bewley et al., 1999; Leavitt et al., 2013; Roelvink et al., 1998, 1999; Wu and Nemerow, 2004) and PRD1 (Leavitt et al., 2013) strengthen this hypothesis. For this reason, we undertook kinetic and structural studies of initial attachment of STIV to *Sulfolobus solfataricus* P222, a preferred hyperthermophilic, acidophilic host derived from *Sulfolobus solfataricus* P2 by successive

rounds of isolating infection permissive cells (Ortmann et al., 2008).

Typically, plaque assays are used to determine virus absorption rates to host cells. In our experiments plaque assays proved unreliable. Therefore, we developed a viral adsorption assay in which the number of viral genomes serves as a proxy for the number of infected cells. In this assay, virions were allowed to attach/enter the cells for a defined length of time followed by removal of unbound virus through centrifugation and washing. The remaining tightly bound virus was permitted to complete one replication cycle before the number of viral genomes were measured by qPCR. Assuming virus production correlates directly to the number of infected cells (the same assumption is needed for plaque assay-based determination), this allows relative comparison of the number of infected cells as a function of incubation time. Saturated adsorption was found to occur at 10 min (Figure 4), and the adsorption rate for STIV was  $2 \times 10^{-9} \text{ mL min}^{-1}$  (Table S1). The process was temperature dependent, because binding at room temperature was not observed, even with incubation times up to 1 h. While slower than that reported for other hyperthermophilic archaeal viruses, such as SMV1 and SIRV2, it is faster than rates observed for halophilic archaeal viruses (Quemin et al., 2013; Svirskaitė et al., 2016; Uldahl et al., 2016), and in line with values for bacteriophage, such as T2 (Puck et al., 1951).

### Initial STIV Attachment to Pili

Following incubation of host cells with STIV, virus was observed bound to host pili in both negative stain and cryoelectron micrographs (Figures 4 and S5). The pili were highly flexible and showed an average diameter of 7 nm measured directly from micrographs. These pili resemble the “thread” structures observed on the surface of *Sulfolobus acidocaldarius* (Henche et al., 2012).

### Attachment Is Mediated by the Second and Third Domains of C381

CET was employed to achieve a 3D reconstruction of the STIV-pili interaction. The tomograms localized the point of contact between STIV and the pili at the viral turrets. Interestingly, a single virion was frequently observed to bind multiple pili (Figure 5, Video S1).

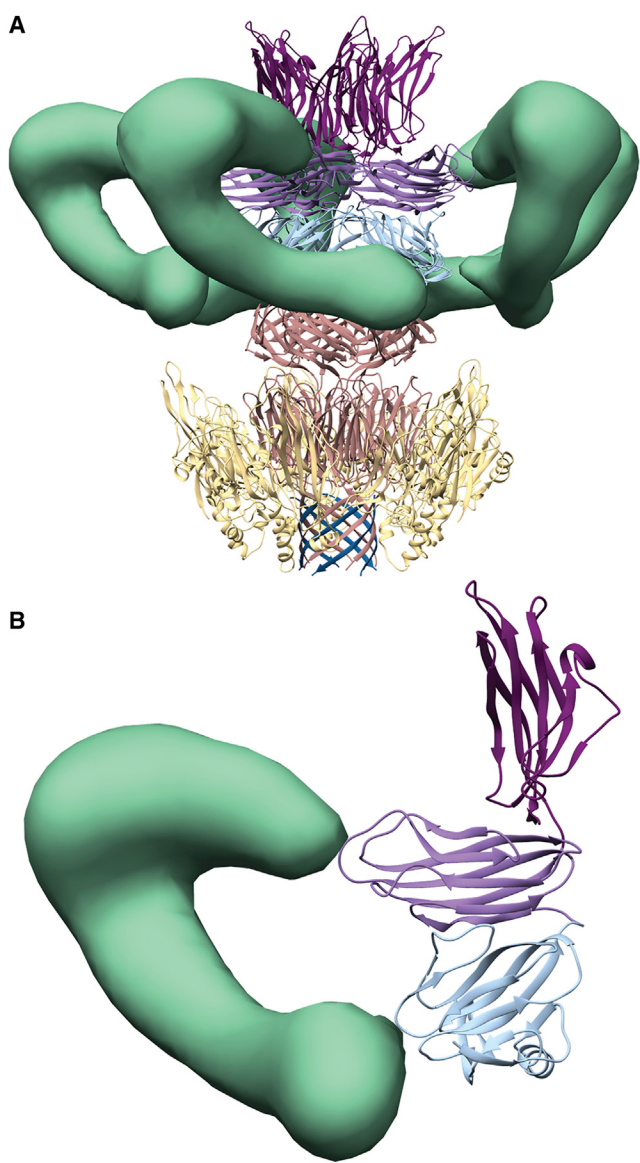


**Figure 3. C381 Petal Protein Interactions**

(A) A difference map for the turret petals, thought to be formed by the C557 protein, is shown in green juxtaposed to the atomic structure of the C381 turret protein. The view of C381 is “opposite” that in Figure 1, with the CHEF sheet of each domain toward the reader (instead of BIDG). The coloring scheme is the same as in Figure 1C, except that the B345 major capsid protein subunits immediately surrounding the turret are shown in wheat to illustrate the location of the capsid shell.

(B) Density from the petal protein intersects the D<sub>1</sub>E<sub>1</sub> and D<sub>2</sub>E<sub>2</sub> loops of C381. See also Figures S3 and S4.

Subtomographic averages of the STIV/pilus interaction were pursued to realize a higher-resolution structure that would allow us to leverage the existing atomic structures of C381 and the entire STIV virion to obtain a pseudo-atomic model for the STIV/pilus complex. Two approaches to subtomographic averaging were taken. In the first approach, subvolume averages were separately calculated for the pili and for the virus particles, which were also averaged over their icosahedral symmetry. The

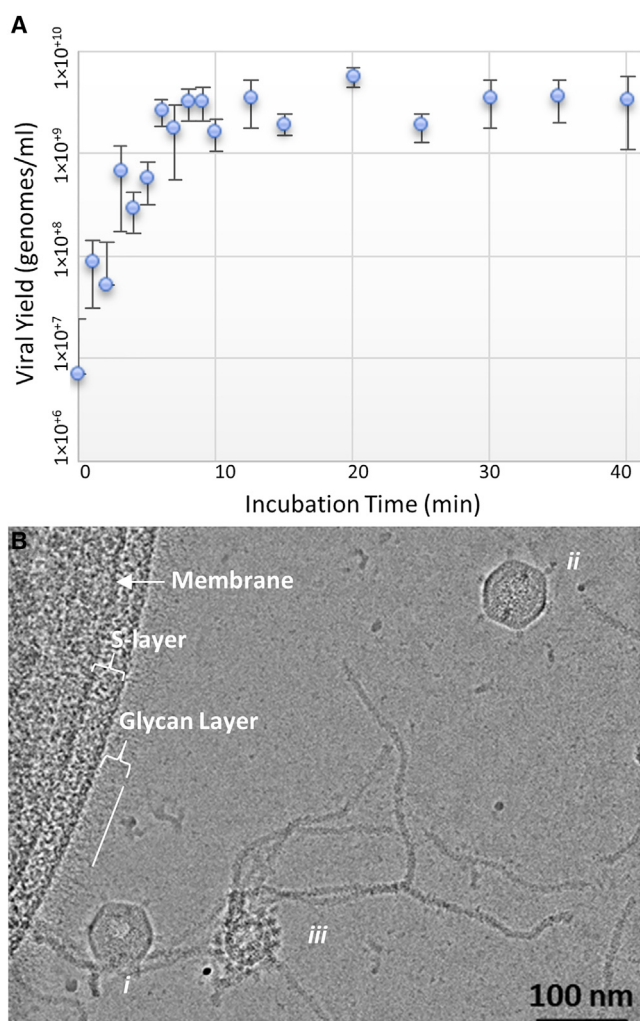


**Figure 4. Initial STIV Attachment**

(A) Kinetics of viral attachment were determined by incubating virus and cells at 80°C for the specified time, then pelleting and washing cells, and quantitating viral infection by qPCR. Initial binding was complete within 10 min. See also Table S1.

(B) Cryo-EM micrograph taken at 0.2 μm underfocus with the Volta phase plate revealed STIV bound to host pili (particles i and ii). The lipid membrane and outer surface layer of the *Sulfolobus* host are also apparent (white arrow and small bracket, respectively). The surface layer is heavily decorated with a lawn or network of very fine filaments that likely represent an extensive glycan layer more than 30 nm thick (white bracket and line). A third particle that may represent degraded or disassembled virus is also present (iii). See also Figure S5.

viral and pilus subvolume averages were then redistributed across the tomogram in their refined locations and orientation to give a composite model (Figure 5B). The six averaged STIV particles yielded a 2.0-nm resolution STIV structure as judged by a 0.143 Fourier shell correlation cutoff when compared with the 3.9-Å STIV single-particle structure (Veesler et al., 2013) (Figure S6). Averaging of host pili resulted in a cylindrical density 6 nm in diameter. Consistent with the lack of structural detail for the helices in single-exposure micrographs, we were unable to resolve the helical sense and pitch of the pili, resulting in a

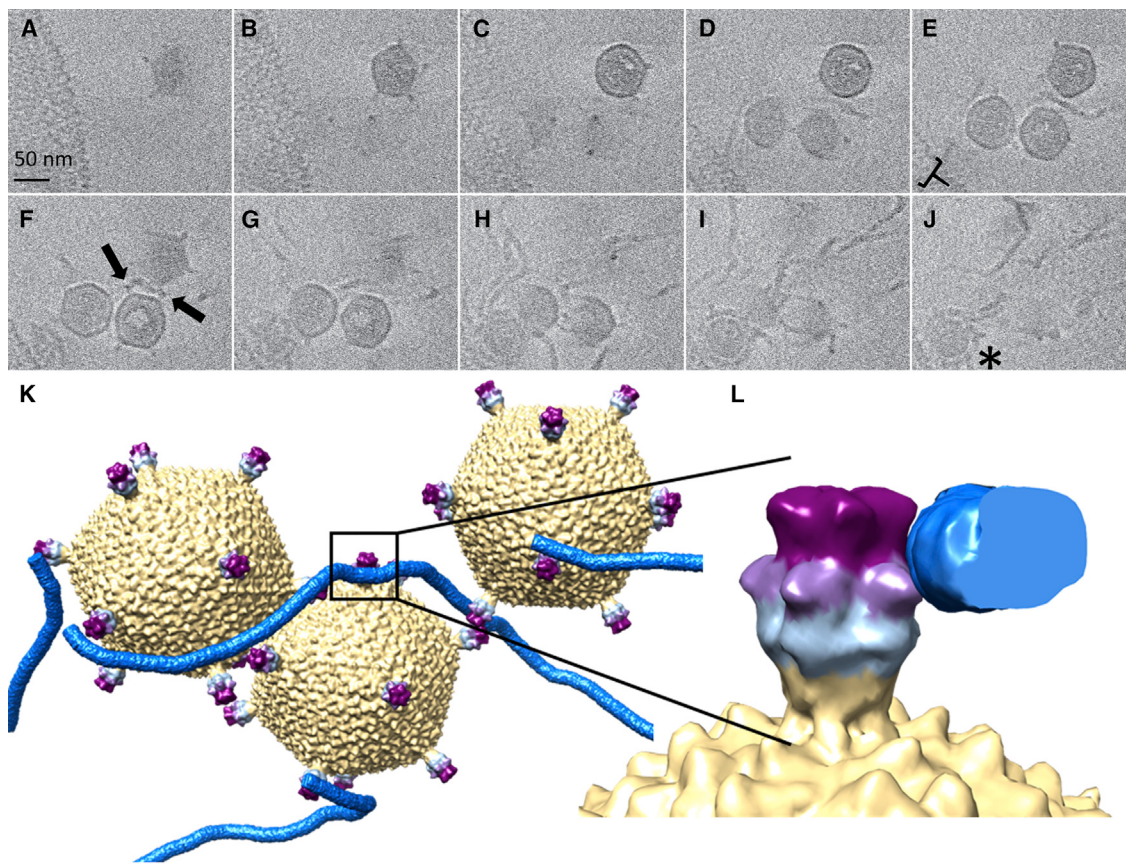


**Figure 5. Tomographic Structure of the STIV Pilus Interaction**

(A–J) Sections (2.25 nm thick) at 10-nm spacings through a representative tomogram of STIV bound to host pili. Black arrows indicate binding sites between virus and pili. Three intact virions are visible along with a fourth degraded or disassembled particle (asterisk in J). The cell edge is visible along the left and lower left of the sections; the surface layer is marked by a bracket in (E).

(K) The subvolume averages for the three virions and the pili are shown in their relative locations and orientations within a tomogram. The point of interaction between the virion and pilus is always at the viral turret.

(L) An enlarged view of the turret highlighted in (K) rotated 90° about the vertical axis and looking into a cross-section through the pilus. The C381 turret protein is colored light, medium, and dark purple to indicate the position of the first, second and third jelly roll domains of the protein, respectively. Pilus recognition is mediated by second and third domains of C381. Scale bar (A), 50 nm. See also [Video S1](#).

low-resolution envelope for the pili. However, this approach did clearly allow localization of the pili with respect to the viral turrets. In all virus turret interactions in the tomograms, the viral turret uses the cleft between the second and third domains of C381 to recognize the host pili ([Figure 5; Video S1](#)).

In a second, complementary strategy, candidate turret-fiber interactions identified in the composite model described above were aligned and averaged. The entire capsid was used to align the turret of interest along the  $y$  axis. This effectively solved for theta and psi and left only five possibilities for phi. Rotation in fixed 72° increments then explored the five possibilities for each candidate interaction. The final average contained ten turret-pilus interactions and displayed strong density on one side of the viral turret indicating the region of pilus binding ([Figure 6A](#)). As expected, density reinforces only near the turret, since the pili appear highly flexible and their paths quickly diverge, both before and after the point of contact.

To highlight the density contribution of the pilus, a difference map was calculated by subtracting the STIV density from the

ten-particle turret-pilus average. The location of the resultant difference density relative to the single-particle reconstruction of STIV and the hybrid molecular model are shown in [Figure 6B](#). In agreement with the composite model described above, the strongest pilus density from the difference map lies between the second and third domains of a single subunit of the C381 pentamer. Regardless of the strategy used for subtomographic averaging, when the STIV atomic model is fit within the averaged density, specific regions of C381 are implicated in pilus recognition ([Figure 7; Video S1](#)). Both models suggest that domain 2 uses strand F<sub>2</sub>, the F<sub>2</sub>G<sub>2</sub> edge of the  $\beta$  sandwich and the F<sub>2</sub>G<sub>2</sub> loop, and that domain 3 uses strand C<sub>3</sub> and the B<sub>3</sub>C<sub>3</sub> edge of the  $\beta$  sandwich to bind host pili. Surface-exposed, strictly conserved residues lie within these regions and potentially mediate recognition of the pili. These include Asn196 and Ser215 in domain 2, and Glu285 and Asn289 in domain 3. Highly conserved residues Gln274 and Gln291 may also be involved. Notably, the pilus binding site appears to occlude the petal binding site in domain 2, suggesting that binding of petal protein

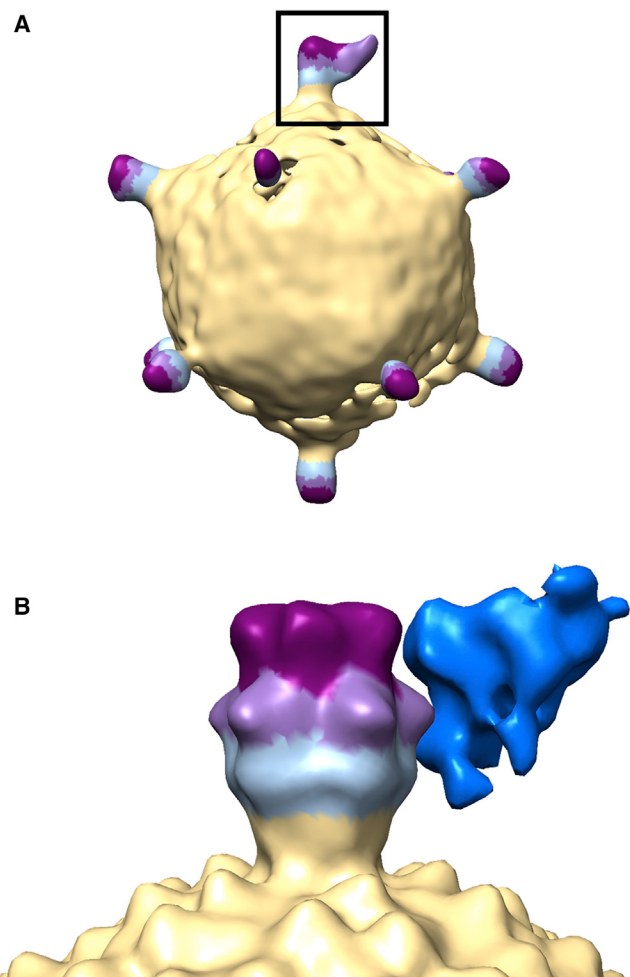


**Figure 6. Sub-tomogram Average of Ten STIV-Pili Interactions**

(A) Each turret-pilus interaction was rotated to a standard orientation with the interacting turret along the y axis (top turret, square). Each subvolume was then rotated about y ( $\phi$ ) in  $72^\circ$  increments to orient all pilus bound sites. Unlike strategy 1, the virus particle has not been averaged over the icosahedral symmetry. Duck bill-shaped density for the pilus at the pilus/turret contact is seen along the right side of the top of the turret (black square).

(B) A difference map (STIV/Pilus-STIV) was then calculated to highlight the new density due to pilus—dark blue density, right side of (B). This difference density is juxtaposed against the six-particle icosahedral average of the tomographic virions, in which the STIV turret is colored by domain (light blue, light purple, dark purple/domains 1, 2, and 3). A 10 SD Gaussian filter was applied to generate the map in (A), whereas a 5 SD Gaussian filter was applied in (B), thus the additional features.

C557 and pilus are mutually exclusive, and that the petal bound form of STIV would thus be non-infectious.

## DISCUSSION

### C557 Petal Protein Is a Maturation Factor

It is clear that turrets fully decorated with petals would be unable to bind host pili. This suggests that the petal protein, tentatively identified as C557 (Khayat et al., 2010; Maaty et al., 2006; Rice et al., 2004), functions as a maturation protein. In this role, newly released virions would contain petal protein at near full

occupancy, preventing re-binding to pili on the infected (lysed) cell. Later these petals would dissociate, priming the virus for attachment to pili on a new host cell.

### An S-Layer Glycan Barrier

Most studied Archaea are wrapped in a proteinaceous, para-crystalline S-layer (Albers and Meyer, 2011; Klingl, 2014). An unanticipated outcome of this study is the observation in cryo-EM micrographs of a massive lawn, or network of ultra-thin filaments extending  $40\ \mu\text{m}$  ( $400\ \text{\AA}$ ) or more from the proteinaceous S-layer. The S-layers in general, and *Sulfolobus* species specifically, are known to be heavily glycosylated (Albers and Meyer, 2011; Jarrell et al., 2014; Klingl, 2014). However, visualized in the context of STIV infection, the magnitude of the glycan barrier that must be overcome by an invading virus becomes much clearer. Not only must the virion traverse or circumvent the proteinaceous component of the S-layer and subsequent membrane, it must also first traverse (or circumvent) this substantial glycan exo-layer as well. Indeed, one of the virions (particle i) in Figure 4B appears immediately adjacent to this external glycan barrier.

### Type IV Pili

The outstanding question of the identity of the filaments recognized by STIV remains. Initial attempts to shear virus bound particles from the cell surface to identify the STIV receptor have so far proved unsuccessful. However, the literature contains important clues to their identity. Albers and coworkers report that the most widespread archaeal surface structures show homology to type IV pili (Chaudhury et al., 2018). The functions of such filaments are diverse, ranging from motility and adhesion to DNA exchange. They are also diverse in diameter, with the archaeal flagella, or archaellum, showing a diameter of  $10\text{--}15\ \text{nm}$ , type IV adhesive pili with diameters of  $7\text{--}15\ \text{nm}$ , and Ups pili at  $10\ \text{nm}$ . And while the high abundance of type IV pili is a hallmark of Archaea, several unique non-type IV pili are also known in Archaea, including cannulae, hami, and fimbriae, which are thought to play roles in building cellular networks and biofilm formation (Chaudhury et al., 2018). Of these, the STIV bound filaments appear too small to correspond to the archaellum or cannulae; and, although small changes in molecular composition can have significant effects on the diameter of such filaments, they also appear too small to correspond to an Mth-like fimbriae. Furthermore, to our knowledge, hami have not been reported in *S. solfataricus*. Finally, the recently published pilus structure from *S. islandicus* has a slightly smaller diameter at  $5\ \text{nm}$  (Wang et al., 2019). This pilus is encoded by *SiL\_2606* and mediates initial attachment for SIRV2. The *S. solfataricus* P2 genome encodes a homologous gene, *SSO2146*, with 84% identity. Furthermore, both *SiL\_2606* and the pili recognized by STIV1 appear similar in their degree of flexibility. Still, using the purification methods of Wang et al. (2019) we have been unable to isolate the pili separate from the host cells, which may indicate that they are separate structures. Thus, we speculate that initial STIV attachment is a type IV pilus-like structure on the *Sulfolobus* surface, but its identity remains unknown.

### Host Discrimination

The structural analysis presented here clearly implicates the prominent turrets of STIV-1, and the second and third domains of C381 in particular, in receptor binding and host recognition.

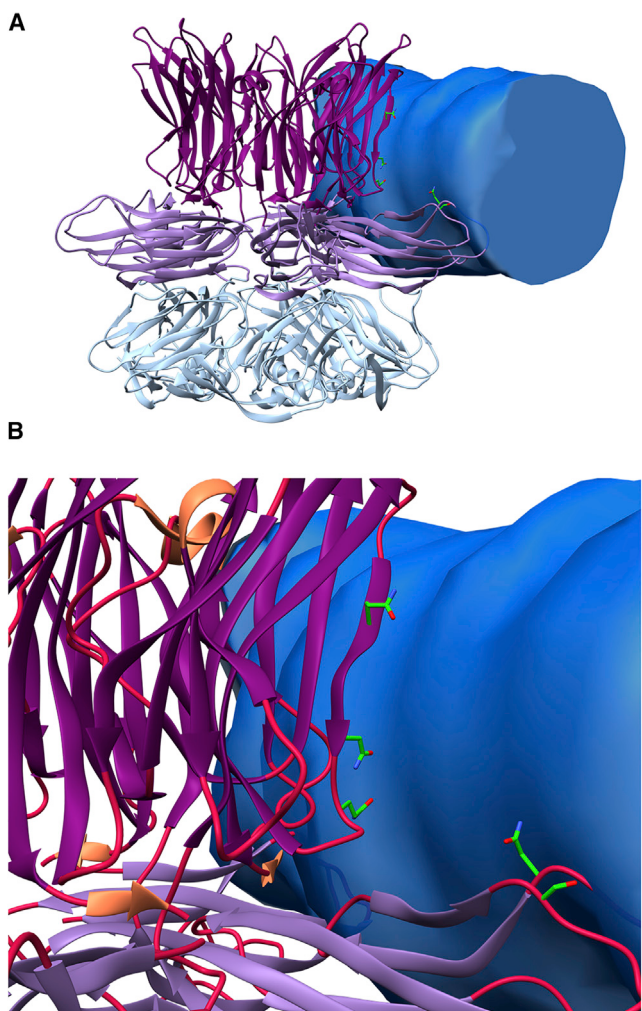


**Figure 7. Pilus Recognition by C381**

(A) Domain 2 uses strand F<sub>2</sub> and the F<sub>2</sub>G<sub>2</sub> edge of the β sandwich and the F<sub>2</sub>G<sub>2</sub> and H<sub>2</sub>I<sub>2</sub> loops, while domain 3 uses strand C<sub>3</sub> and the B<sub>3</sub>C<sub>3</sub> edge of the β sandwich to bind host pili. In this model the F<sub>2</sub>G<sub>2</sub> loop intrudes into the pilus density. Modest conformational changes in C381 or surface features of the filament not visible at this resolution likely accommodate the interaction.  
(B) Surface-exposed, strictly conserved residues lie within these regions and potentially mediate recognition of the pili. These include Asn196 and Ser215 in domain 2, and Glu285 and Asn289 in domain 3. Highly conserved Gln274 may also be involved.

See also [Video S1](#), [Figure S3](#), [Data S1](#) and [S2](#).

In this light, sequence divergence between the STIV-1 and STIV-2 clades of C381, and the lack of conservation in surface residues implicated in receptor recognition between these clades could indicate use of different type IV pili, resulting in host discrimination. This is supported by examination of a micrograph in which STIV-2 co-purified with host flagellar-like filaments ([Happonen et al., 2010](#)). These flagella appear thicker and more rigid than the pili recognized by STIV-1.

### Genome Delivery

We currently lack detailed information on the mechanism employed by any archaeal virus to deliver its genome into the host

cell. However, we do know that initial binding to cellular appendages such as type IV pili and flagella are an emerging theme for archaeal viruses. For example, the ravidivirus SIRV2 binds to the tip of an unknown type IV pilus-like structure ([Deng et al., 2014](#); [Quemin et al., 2013](#)). At later time points SIRV2 is found in bits and pieces localized on the cell surface. How it migrates from the tip of the pili to the cell surface is unknown. We face a similar question now for STIV-1. Were the unknown pili able to retract ([Poranen et al., 2002](#)), this could certainly explain the presence of particle i in [Figure 4B](#). However, retractile pili have not yet been observed in the Archaea ([Chaudhury et al., 2018](#)). An alternative mechanism is a random or directional walk along the pili until it encounters the cell surface, i.e., the classic “nut on a bolt” hypothesis in which phage move along a pilus to the cell body, presumably directed in their motion by the “threads,” or twist and rise of the pilus ([Berg and Anderson, 1973](#); [Samuel et al., 1999](#)). However, in this work STIV was most frequently observed bound to multiple pili, as its icosahedral symmetry makes it a multivalent particle. In this context, the nut on a blot model seems less viable for this system. A third alternative is that the virus might bind and become entangled in multiple pili, and like a burr in a dog’s coat that stochastically works its way through the fur until it’s entangled and trapped against the skin, STIV might bind multiple pili as it works its way toward the cell surface. Clearly, additional data at both earlier and later time points are needed to distinguish among these and other possibilities.

Isolated archaeal viruses frequently possess lipid envelopes, and of the 18 archaeal virus families, 11 are enveloped ([Atanassova et al., 2015](#); [Liu et al., 2017](#); [Prangishvili et al., 2018](#); [Rensen et al., 2016](#); [Wagner et al., 2017](#)). In the case of STIV, it is an internal lipid envelope ([Figure 1](#)). This raises the question of how the genome transits both the host and the viral membranes. As a member of the PRD1 viral lineage, we consider the possibility that genome delivery might be similar to other members of this lineage utilizing an internal lipid membrane within an icosahedral shell. Remarkably, following initial receptor attachment in PRD1, the internal membrane “vesicle” in this phage is observed to develop a tube-like structure that extends through the unique vertex of PRD1 and into the host cell membrane, providing a conduit for transfer of the viral genome into the host cell ([Mantynen et al., 2019](#); [Peralta et al., 2013](#)). For STIV-1, we can consider that following localization to the cell surface, secondary receptor binding sites on STIV-1 could be engaged (perhaps unmasked by conformational changes upon recognition of the type IV pilus), catalyzing a similar transformation for STIV-1 with subsequent genome insertion.

Alternatively, PM2, also a member of the PRD1 viral lineage housing an internal membrane, is thought to bind to a cell surface receptor, upon which the protein capsid dissociates, revealing the viral envelope and promoting fusion with the host cell membrane ([Kivela et al., 2004](#); [Mantynen et al., 2019](#)). This model requires disassembly of a presumably metastable viral capsid. Interestingly, disassembled states of STIV-1 have been observed ([Khayat et al., 2010](#)), and an entangled virus in the process of disassembly may be visible in [Figure 4](#) (particle iii), although this might just as well represent a damaged particle present in the purified virus used for these experiments, or an unsuccessful dead end in the infection process due to entrapment in multiple pili. Regardless,

from the structural perspective, the C381 subunit interfaces are surprisingly hydrophilic, and recombinantly expressed C381 is a well-behaved monomer before crystallization, as are the major capsid protein (B345) and the penton base (A223). From the thermodynamic view, this is consistent with the idea of a metastable icosahedral shell that might spontaneously dissociate upon interaction with cellular receptors. Indeed, in addition to serving as a maturation protein that prevents readsorption to an infected cell, the C557 petal protein may also serve to pre-organize C381 for assembly into the virion, and then dissociate once the virus emerges into the acidified hot spring.

However, if a disassembly mechanism is used, this raises additional questions. Does the membrane-enclosed genome enter the cell by endocytosis, direct injection through the A55/A223  $\alpha$ -hemolysin-like structure, or by a fusion event such as that suggested for *Sulfolobus monocaudavirus* (Uldahl et al., 2016). Critically, with regard to endocytosis or membrane fusion, the hyperthermophilic membranes in *S. solfataricus* and STIV are composed of cyclic tetra-ether lipids that span the entire membrane (Boyd et al., 2013; Maaty et al., 2006; van de Vossenberg et al., 1998). These membranes lack the inner and outer leaflets found in mesophilic organisms. Thus, if membrane fusion is involved, we anticipate a fundamentally different process than current models for fusion of lipid bilayers (Harrison, 2008). Regardless of the mechanism of genome delivery, we are greatly interested to study these later points in STIV attachment and entry. Such studies have clear potential to make fundamental contributions to our understanding of membrane dynamics, archaeal biology, and life on Earth.

## STAR★METHODS

Detailed methods are provided in the online version of this paper and include the following:

- KEY RESOURCES TABLE
- LEAD CONTACT AND MATERIALS AVAILABILITY
- EXPERIMENTAL MODEL AND SUBJECT DETAILS
- METHOD DETAILS
  - Quantification of Viral Attachment
  - Phylogenetic Tree and Identification of Conserved Residues in C381
  - Expression, Purification and Crystallization of C381
  - C381 Crystallographic Structure Determination
  - Negative Stain Electron Microscopy
  - Cryo-Electron Tomography
  - Subvolume Alignment and Averaging for STIV
  - Subvolume Alignment and Averaging for Pili
  - Subvolume Alignment and Averaging of the Turret/Pilus Interaction
  - Fitting the Atomic Structure of STIV into the Subvolume Average
- QUANTIFICATION AND STATISTICAL ANALYSIS
- DATA AND CODE AVAILABILITY

## SUPPLEMENTAL INFORMATION

Supplemental Information can be found online at <https://doi.org/10.1016/j.str.2019.09.005>.

## ACKNOWLEDGMENTS

C.M.L. expresses his sincere appreciation to Professor Wolfgang Baumeister for the opportunity to do sabbatical work at the Max-Planck Institute of Biochemistry where the cryo-ET data were collected. This work was supported by the National Science Foundation, grants DEB-1342876 to M.J.Y. and MCB-1413534 to C.M.L.

## AUTHOR CONTRIBUTIONS

Conceptualization, C.M.L.; Methodology, R.H., B.J.E., D.B., M.J.Y., and C.M.L.; Investigation, R.H., B.J.E., D.B., M.J.Y., and C.M.L.; Formal Analysis, R.H., B.J.E., J.H.M.-McG., and C.M.L.; Writing – Original Draft, R.H., B.J.E., M.J.Y., and C.M.L.; Writing – Review & Editing, R.H., D.B., H.E., M.J.Y., and C.M.L.; Funding Acquisition, M.J.Y. and C.M.L.; Resources, H.E., M.J.Y., and C.M.L.; Supervision, H.E., M.J.Y., and C.M.L.

## DECLARATION OF INTERESTS

The authors declare no competing interests.

Received: May 22, 2019

Revised: August 21, 2019

Accepted: September 16, 2019

Published: October 3, 2019

## REFERENCES

- Abbott, S., Iudin, A., Korir, P.K., Somasundharam, S., and Patwardhan, A. (2018). EMDB web resources. *Curr. Protoc. Bioinformatics* 61, 5 10 11–15 10 12.
- Adam, P.S., Borrel, G., Brochier-Armanet, C., and Gribaldo, S. (2017). The growing tree of Archaea: new perspectives on their diversity, evolution and ecology. *ISME J.* 11, 2407–2425.
- Adams, P.D., Afonine, P.V., BunkOczi, G., Chen, V.B., Davis, I.W., Echols, D.N., Headd, J.J., Hung, L.-W., Kapral, G.J., Grosse-Kunstleve, R.W., et al. (2010). PHENIX: a comprehensive Python-based system for macromolecular structure solution. *Acta Crystallogr. D Biol. Crystallogr.* D66, 213–221.
- Adams, P.D., Baker, D., Brunger, A.T., Das, R., DiMaio, F., Read, R.J., Richardson, D.C., Richardson, J.S., and Terwilliger, T.C. (2013). Advances, interactions, and future developments in the CNS, Phenix, and Rosetta structural biology software systems. *Annu. Rev. Biophys.* 42, 265–287.
- Albers, S.V., and Meyer, B.H. (2011). The archaeal cell envelope. *Nat. Rev. Microbiol.* 9, 414–426.
- Altschul, S.F., Madden, T.L., Schaffer, A.A., Zhang, J., Zhang, Z., Miller, W., and Lipman, D.J. (1997). Gapped BLAST and PSI-BLAST: a new generation of protein database search programs. *Nucleic Acids Res.* 25, 3389–3402.
- Atanasova, N.S., Sencilo, A., Pietila, M.K., Roine, E., Oksanen, H.M., and Bamford, D.H. (2015). Comparison of lipid-containing bacterial and archaeal viruses. *Adv. Virus Res.* 92, 1–61.
- Bautista, M.A., Zhang, C., and Whitaker, R.J. (2015). Virus-induced dormancy in the archaeon *Sulfolobus islandicus*. *MBio* 6, <https://doi.org/10.1128/mBio.02565-14>.
- Berg, H.C., and Anderson, R.A. (1973). Bacteria swim by rotating their flagellar filaments. *Nature* 245, 380–382.
- Bergelson, J.M., Cunningham, J.A., Droguett, G., Kurt-Jones, E.A., Krithivas, A., Hong, J.S., Horwitz, M.S., Crowell, R.L., and Finberg, R.W. (1997). Isolation of a common receptor for Coxsackie B viruses and adenoviruses 2 and 5. *Science* 275, 1320–1323.
- Bewley, M.C., Springer, K., Zhang, Y.B., Freimuth, P., and Flanagan, J.M. (1999). Structural analysis of the mechanism of adenovirus binding to its human cellular receptor, CAR. *Science* 286, 1579–1583.
- Bhardwaj, A., Molineux, I.J., Casjens, S.R., and Cingolani, G. (2011). Atomic structure of bacteriophage Sf6 tail needle knob. *J. Biol. Chem.* 286, 30867–30877.

- Bolduc, B., Wirth, J., Mazurie, A., and Young, M. (2015). Viral assemblage composition in Yellowstone acidic hot springs assessed by network analysis. *ISME J.* 9, 2162–2177.
- Boyd, E.S., Hamilton, T.L., Wang, J., He, L., and Zhang, C.L. (2013). The role of tetraether lipid composition in the adaptation of thermophilic archaea to acidity. *Front Microbiol.* 4, 62.
- Brumfield, S.K., Ortmann, A.C., Ruigrok, V., Suci, P., Douglas, T., and Young, M.J. (2009). Particle assembly and ultrastructural features associated with replication of the lytic archaeal virus *Sulfolobus* turreted icosahedral virus. *J. Virol.* 83, 5964–5970.
- Camacho, C., Coulouris, G., Avagyan, V., Ma, N., Papadopoulos, J., Bealer, K., and Madden, T.L. (2009). BLAST+: architecture and applications. *BMC Bioinformatics* 10, 421.
- Chaudhury, P., Quax, T.E.F., and Albers, S.V. (2018). Versatile cell surface structures of archaea. *Mol. Microbiol.* 107, 298–311.
- Danev, R., and Baumeister, W. (2017). Expanding the boundaries of cryo-EM with phase plates. *Curr. Opin. Struct. Biol.* 46, 87–94.
- Danev, R., Buijsse, B., Khoshouei, M., Plitzko, J.M., and Baumeister, W. (2014). Volta potential phase plate for in-focus phase contrast transmission electron microscopy. *Proc. Natl. Acad. Sci. U S A.* 111, 15635–15640.
- Davis, I.W., Murray, L.W., Richardson, J.S., and Richardson, D.C. (2004). MOLPROBITY: structure validation and all-atom contact analysis for nucleic acids and their complexes. *Nucleic Acids Res.* 32, W615–W619.
- Davis, I.W., Leaver-Fay, A., Chen, V.B., Block, J.N., Kapral, G.J., Wang, X., Murray, L.W., Arendall, W.B., 3rd, Snoeyink, J., Richardson, J.S., et al. (2007). MolProbity: all-atom contacts and structure validation for proteins and nucleic acids. *Nucleic Acids Res.* 35, W375–W383.
- Dellas, N., Snyder, J.C., Dills, M., Nicolay, S.J., Kerchner, K.M., Brumfield, S.K., Lawrence, C.M., and Young, M.J. (2015). Structure-based mutagenesis of *Sulfolobus* turreted icosahedral virus B204 reveals essential residues in the virion-associated DNA-packaging ATPase. *J. Virol.* 90, 2729–2739.
- DeLong, E.F., and Pace, N.R. (2001). Environmental diversity of bacteria and archaea. *Syst. Biol.* 50, 470–478.
- Deng, L., He, F., Bhoobalan-Chitty, Y., Martinez-Alvarez, L., Guo, Y., and Peng, X. (2014). Unveiling cell surface and type IV secretion proteins responsible for archaeal ravidivirus entry. *J. Virol.* 88, 10264–10268.
- Edgar, R.C. (2004). MUSCLE: multiple sequence alignment with high accuracy and high throughput. *Nucleic Acids Res.* 32, 1792–1797.
- Emsley, P., and Cowtan, K. (2004). Coot: model-building tools for molecular graphics. *Acta Crystallogr. Section D* 60, 2126–2132.
- Falkowski, P.G., Fenchel, T., and Delong, E.F. (2008). The microbial engines that drive Earth's biogeochemical cycles. *Science* 320, 1034–1039.
- Fu, C.Y., and Johnson, J.E. (2012). Structure and cell biology of archaeal virus STIV. *Curr. Opin. Virol.* 2, 122–127.
- Fu, C.Y., Wang, K., Gan, L., Lanman, J., Khayat, R., Young, M.J., Jensen, G.J., Doerschuk, P.C., and Johnson, J.E. (2010). In vivo assembly of an archaeal virus studied with whole-cell electron cryotomography. *Structure* 18, 1579–1586.
- Fukuda, Y., Laugks, U., Lucic, V., Baumeister, W., and Danev, R. (2015). Electron cryotomography of vitrified cells with a Volta phase plate. *J. Struct. Biol.* 190, 143–154.
- Fulton, J., Bothner, B., Lawrence, M., Johnson, J.E., Douglas, T., and Young, M. (2009). Genetics, biochemistry and structure of the archaeal virus STIV. *Biochem. Soc. Trans.* 37, 114–117.
- Goulet, A., Vestergaard, G., Felisberto-Rodrigues, C., Campanacci, V., Garrett, R.A., Cambillau, C., and Ortiz-Lombardia, M. (2010). Getting the best out of long-wavelength X-rays: de novo chlorine/sulfur SAD phasing of a structural protein from ATV. *Acta Crystallogr. D* 66, 304–308.
- Happonen, L.J., Redder, P., Peng, X., Reigstad, L.J., Prangishvili, D., and Butcher, S.J. (2010). Familial relationships in hyperthermo- and acidophilic archaeal viruses. *J. Virol.* 84, 4747–4754.
- Harrison, S.C. (2008). Viral membrane fusion. *Nat. Struct. Mol. Biol.* 15, 690–698.
- Harrison, S.C., Olson, A.J., Schutt, C.E., Winkler, F.K., and Bricogne, G. (1978). Tomato bushy stunt virus at 2.9 Å resolution. *Nature* 276, 368–373.
- Henche, A.L., Ghosh, A., Yu, X., Jeske, T., Egelman, E., and Albers, S.V. (2012). Structure and function of the adhesive type IV pilus of *Sulfolobus acidocaldarius*. *Environ. Microbiol.* 14, 3188–3202.
- Heumann, J.M., Hoenger, A., and Mastronarde, D.N. (2011). Clustering and variance maps for cryo-electron tomography using wedge-masked differences. *J. Struct. Biol.* 175, 288–299.
- Hochstein, R., Bollschweiler, D., Engelhardt, H., Lawrence, C.M., and Young, M. (2015). Large tailed spindle viruses of archaea: a new way of doing viral business. *J. Virol.* 89, 9146–9149.
- Hochstein, R., Bollschweiler, D., Dharmavaram, S., Lintner, N.G., Plitzko, J.M., Bruinsma, R., Engelhardt, H., Young, M.J., Klug, W.S., and Lawrence, C.M. (2018). Structural studies of *Acidianus* tailed spindle virus reveal a structural paradigm used in the assembly of spindle-shaped viruses. *Proc. Natl. Acad. Sci. U S A.* 115, 2120–2125.
- Holm, L., and Rosenstrom, P. (2010). DALI server: conservation mapping in 3D. *Nucleic Acids Res.* 38, W545–W549.
- Jarrell, K.F., Ding, Y., Meyer, B.H., Albers, S.V., Kaminski, L., and Eichler, J. (2014). N-linked glycosylation in Archaea: a structural, functional, and genetic analysis. *Microbiol. Mol. Biol. Rev.* 78, 304–341.
- Jones, T.A. (1992). A, yaap, asap, @#\*? A set of averaging programs. In Molecular Replacement, E.J. Dodson, S. Gover, and W. Wolf, eds. (SERC Daresbury Laboratory), pp. 91–105.
- Karner, M.B., DeLong, E.F., and Karl, D.M. (2001). Archaeal dominance in the mesopelagic zone of the Pacific Ocean. *Nature* 409, 507–510.
- Khayat, R., Tang, L., Larson, E.T., Lawrence, C.M., Young, M., and Johnson, J.E. (2005). Structure of an archaeal virus capsid protein reveals a common ancestry to eukaryotic and bacterial viruses. *PNAS* 102, 18944–18949.
- Khayat, R., Fu, C.Y., Ortmann, A.C., Young, M.J., and Johnson, J.E. (2010). The architecture and chemical stability of the archaeal *Sulfolobus* turreted icosahedral virus. *J. Virol.* 84, 9575–9583.
- Khoshouei, M., Pfeffer, S., Baumeister, W., Forster, F., and Danev, R. (2017). Subtomogram analysis using the Volta phase plate. *J. Struct. Biol.* 197, 94–101.
- Kivela, H.M., Daugelavicius, R., Hankkio, R.H., Bamford, J.K., and Bamford, D.H. (2004). Penetration of membrane-containing double-stranded-DNA bacteriophage PM2 into *Pseudoalteromonas* hosts. *J. Bacteriol.* 186, 5342–5354.
- Kleywegt, G.J., and Read, R.J. (1997). Not your average density. *Structure* 5, 1557–1569.
- Klingl, A. (2014). S-Layer and cytoplasmic membrane—exceptions from the typical archaeal cell wall with a focus on double membranes. *Front Microbiol.* 5, 624.
- Kraft, P., Kummel, D., Oeckinghaus, A., Gauss, G.H., Wiedenheft, B., Young, M., and Lawrence, C.M. (2004). Structure of D-63 from *Sulfolobus* spindle-shaped virus 1: surface properties of the dimeric four-helix bundle suggest an adaptor protein function. *J. Virol.* 78, 7438–7442.
- Kremer, J.R., Mastronarde, D.N., and McIntosh, J.R. (1996). Computer visualization of three-dimensional image data using IMOD. *J. Struct. Biol.* 116, 71–76.
- Krissinel, E., and Henrick, K. (2007). Inference of macromolecular assemblies from crystalline state. *J. Mol. Biol.* 372, 774–797.
- Kumar, S., Stecher, G., Li, M., Knyaz, C., and Tamura, K. (2018). MEGA X: molecular evolutionary genetics analysis across computing platforms. *Mol. Biol. Evol.* 35, 1547–1549.
- Larkin, M.A., Blackshields, G., Brown, N.P., Chenna, R., McGgettigan, P.A., McWilliam, H., Valentin, F., Wallace, I.M., Wilm, A., Lopez, R., et al. (2007). Clustal W and Clustal X version 2.0. *Bioinformatics* 23, 2947–2948.
- Larson, E.T., Reiter, D., Young, M., and Lawrence, C.M. (2006). Structure of A197 from *Sulfolobus* turreted icosahedral virus: a crenarchaeal viral glycosyltransferase exhibiting the GT-A fold. *J. Virol.* 80, 7636–7644.

- Larson, E.T., Eilers, B., Menon, S., Reiter, D., Ortmann, A., Young, M.J., and Lawrence, C.M. (2007). A winged-helix protein from *Sulfolobus* turreted icosahedral virus points toward stabilizing disulfide bonds in the intracellular proteins of a hyperthermophilic virus. *Virology* 368, 249–261.
- Lawrence, C.M., Menon, S., Eilers, B.J., Bothner, B., Khayat, R., Douglas, T., and Young, M.J. (2009). Structural and functional studies of archaeal viruses. *J. Biol. Chem.* 284, 12599–12603.
- Leavitt, J.C., Gogokhia, L., Gilcrease, E.B., Bhardwaj, A., Cingolani, G., and Casjens, S.R. (2013). The tip of the tail needle affects the rate of DNA delivery by bacteriophage P22. *PLoS One* 8, e70936.
- Lee, C.C., Ko, T.P., Chou, C.C., Yoshimura, M., Doong, S.R., Wang, M.Y., and Wang, A.H. (2006). Crystal structure of infectious bursal disease virus VP2 subviral particle at 2.6 Å resolution: implications in virion assembly and immunogenicity. *J. Struct. Biol.* 155, 74–86.
- Leininger, S., Urich, T., Schloter, M., Schwark, L., Qi, J., Nicol, G.W., Prosser, J.I., Schuster, S.C., and Schleper, C. (2006). Archaea predominate among ammonia-oxidizing prokaryotes in soils. *Nature* 442, 806–809.
- Lintner, N.G., Frankel, K.A., Tsutakawa, S.E., Alsbury, D.L., Copie, V., Young, M.J., Tainer, J.A., and Lawrence, C.M. (2011). The structure of the CRISPR-associated protein Csa3 provides insight into the regulation of the CRISPR/Cas system. *J. Mol. Biol.* 405, 939–955.
- Lipp, J.S., Morono, Y., Inagaki, F., and Hinrichs, K.U. (2008). Significant contribution of Archaea to extant biomass in marine subsurface sediments. *Nature* 454, 991–994.
- Liu, Y., Ishino, S., Ishino, Y., Pehau-Arnaudet, G., Krupovic, M., and Prangishvili, D. (2017). A novel type of polyhedral viruses infecting hyperthermophilic Archaea. *J. Virol.* 91, <https://doi.org/10.1128/JVI.00589-17>.
- Lloyd-Price, J., Abu-Ali, G., and Huttenhower, C. (2016). The healthy human microbiome. *Genome Med.* 8, 51.
- Maaty, W.S., Ortmann, A.C., Dlakic, M., Schulstad, K., Hilmer, J.K., Liepold, L., Weidenheft, B., Khayat, R., Douglas, T., Young, M.J., et al. (2006). Characterization of the archaeal thermophile *Sulfolobus* turreted icosahedral virus validates an evolutionary link among double-stranded DNA viruses from all domains of life. *J. Virol.* 80, 7625–7635.
- Maaty, W.S., Selvig, K., Ryder, S., Tarlykov, P., Hilmer, J.K., Heinemann, J., Steffens, J., Snyder, J.C., Ortmann, A.C., Movahed, N., et al. (2012). Proteomic analysis of *Sulfolobus solfataricus* during *Sulfolobus* turreted icosahedral virus infection. *J. Proteome Res.* 11, 1420–1432.
- Mantynen, S., Sundberg, L.R., Oksanen, H.M., and Poranen, M.M. (2019). Half a century of research on membrane-containing bacteriophages: bringing new concepts to modern virology. *Viruses* 11, <https://doi.org/10.3390/v11010076>.
- Mastronarde, D.N. (2005). Automated electron microscope tomography using robust prediction of specimen movements. *J. Struct. Biol.* 152, 36–51.
- Menon, S.K., Eilers, B.J., Young, M.J., and Lawrence, C.M. (2010). The crystal structure of D212 from *Sulfolobus* spindle-shaped virus ragged hills reveals a new member of the PD-(D/E)XK nuclease superfamily. *J. Virol.* 84, 5890–5897.
- Moll, R., and Schäfer, G. (1988). Chemiosmotic H<sup>+</sup> cycling across the plasma membrane of the thermoacidophilic archaebacterium *Sulfolobus acidocaldarius*. *FEBS Lett.* 232, 359–363.
- Najmudin, S., Pinheiro, B.A., Prates, J.A., Gilbert, H.J., Romao, M.J., and Fontes, C.M. (2010). Putting an N-terminal end to the *Clostridium thermocellum* xylanase Xyn10B story: crystal structure of the CBM22-1-GH10 modules complexed with xylohexaose. *J. Struct. Biol.* 172, 353–362.
- Nicastro, D., Schwartz, C., Pierson, J., Gaudette, R., Porter, M.E., and McIntosh, J.R. (2006). The molecular architecture of axonemes revealed by cryoelectron tomography. *Science* 313, 944–948.
- Olkkonen, V.M., and Bamford, D.H. (1989). Quantitation of the adsorption and penetration stages of bacteriophage phi 6 infection. *Virology* 171, 229–238.
- Ortmann, A.C., Brumfield, S.K., Walther, J., McInerney, K., Brouns, S.J., van de Werken, H.J., Bothner, B., Douglas, T., van de Oost, J., and Young, M.J. (2008). Transcriptome analysis of infection of the archaeon *Sulfolobus solfataricus* with *Sulfolobus* turreted icosahedral virus. *J. Virol.* 82, 4874–4883.
- Otwinski, Z., and Minor, W. (1997). Processing of X-ray diffraction data collected in oscillation mode. In *Macromolecular Crystallography, Part A*, C. Carter and R. Sweet, eds. (Academic Press), pp. 307–326.
- Peralta, B., Gil-Carton, D., Castano-Diez, D., Bertin, A., Boulogne, C., Oksanen, H.M., Bamford, D.H., and Abrescia, N.G. (2013). Mechanism of membranous tunnelling nanotube formation in viral genome delivery. *PLoS Biol.* 11, e1001667.
- Petersen, E.F., Goddard, T.D., Huang, C.C., Couch, G.S., Greenblatt, D.M., Meng, E.C., and Ferrin, T.E. (2004). UCSF Chimera—a visualization system for exploratory research and analysis. *J. Comput. Chem.* 25, 1605–1612.
- Pina, M., Bize, A., Forterre, P., and Prangishvili, D. (2011). The archeoviruses. *FEMS Microbiol. Rev.* 35, 1035–1054.
- Poranen, M.M., Daugelavicius, R., and Bamford, D.H. (2002). Common principles in viral entry. *Annu. Rev. Microbiol.* 56, 521–538.
- Prangishvili, D., Mochizuki, T., Krupovic, M., and Ictv Report, C. (2018). ICTV virus taxonomy profile: Guttaviridae. *J. Gen. Virol.* 99, 290–291.
- Puck, T.T., Garen, A., and Cline, J. (1951). The mechanism of virus attachment to host cells. I. The role of ions in the primary reaction. *J. Exp. Med.* 93, 65–88.
- Quemin, E.R., Lucas, S., Daum, B., Quax, T.E., Kuhlbrandt, W., Forterre, P., Albers, S.V., Prangishvili, D., and Krupovic, M. (2013). First insights into the entry process of hyperthermophilic archaeal viruses. *J. Virol.* 87, 13379–13385.
- Rensen, E.I., Mochizuki, T., Quemin, E., Schouten, S., Krupovic, M., and Prangishvili, D. (2016). A virus of hyperthermophilic archaea with a unique architecture among DNA viruses. *Proc. Natl. Acad. Sci. U S A.* 113, 2478–2483.
- Rice, G., Tang, L., Stedman, K., Roberto, F., Spuhler, J., Gillitzer, E., Johnson, J.E., Douglas, T., and Young, M. (2004). The structure of a thermophilic archaeal virus shows a double-stranded DNA viral capsid type that spans all domains of life. *PNAS* 101, 7716–7720.
- Richardson, J.S. (1981). The anatomy and taxonomy of protein structure. *Adv. Protein Chem.* 34, 167–339.
- Roelvink, P.W., Lizonova, A., Lee, J.G., Li, Y., Bergelson, J.M., Finberg, R.W., Brough, D.E., Kovacs, I., and Wickham, T.J. (1998). The Coxsackievirus-adenovirus receptor protein can function as a cellular attachment protein for adenovirus serotypes from subgroups A, C, D, E, and F. *J. Virol.* 72, 7909–7915.
- Roelvink, P.W., Mi Lee, G., Einfeld, D.A., Kovacs, I., and Wickham, T.J. (1999). Identification of a conserved receptor-binding site on the fiber proteins of CAR-recognizing adenoviridae. *Science* 286, 1568–1571.
- Rossmann, M.G., Abad-Zapatero, C., Murthy, M.R., Liljas, L., Jones, T.A., and Strandberg, B. (1983). Structural comparisons of some small spherical plant viruses. *J. Mol. Biol.* 165, 711–736.
- Samuel, A.D.T., Pitta, T.P., Ryu, W.S., Danese, P.N., Leung, E.C.W., and Berg, H.C. (1999). Flagellar determinants of bacterial sensitivity to chi-phage. *P Natl. Acad. Sci. USA* 96, 9863–9866.
- Schlenker, C., Goel, A., Tripet, B.P., Menon, S., Willi, T., Dlakic, M., Young, M.J., Lawrence, C.M., and Copie, V. (2012). Structural studies of E73 from a hyperthermophilic archaeal virus identify the "RH3" domain, an elaborated ribbon-helix-helix motif involved in DNA recognition. *Biochemistry* 51, 2899–2910.
- Snyder, J.C., Brumfield, S.K., Peng, N., She, Q., and Young, M.J. (2011). *Sulfolobus* turreted icosahedral virus c92 protein responsible for the formation of pyramid-like cellular lysis structures. *J. Virol.* 85, 6287–6292.
- Snyder, J.C., Brumfield, S.K., Kerchner, K.M., Quax, T.E., Prangishvili, D., and Young, M.J. (2013a). Insights into a viral lytic pathway from an archaeal virus-host system. *J. Virol.* 87, 2186–2192.
- Snyder, J.C., Samson, R.Y., Brumfield, S.K., Bell, S.D., and Young, M.J. (2013b). Functional interplay between a virus and the ESCRT machinery in archaea. *Proc. Natl. Acad. Sci. U S A.* 110, 10783–10787.
- Svirskaitė, J., Oksanen, H.M., Daugelavicius, R., and Bamford, D.H. (2016). Monitoring physiological changes in haloarchaeal cell during virus release. *Viruses* 8, 59.
- Szymczyna, B.R., Taurog, R.E., Young, M.J., Snyder, J.C., Johnson, J.E., and Williamson, J.R. (2009). Synergy of NMR, computation, and X-ray crystallography for structural biology. *Structure* 17, 499–507.

- Thauer, R.K., Kaster, A.K., Seedorf, H., Buckel, W., and Hedderich, R. (2008). Methanogenic archaea: ecologically relevant differences in energy conservation. *Nat. Rev. Microbiol.* **6**, 579–591.
- Uldahl, K.B., Jensen, S.B., Bhoobalan-Chitty, Y., Martinez-Alvarez, L., Papathanasiou, P., and Peng, X. (2016). Life cycle characterization of *Sulfolobus monocaudavirus 1*, an extremophilic spindle-shaped virus with extracellular tail development. *J. Virol.* **90**, 5693–5699.
- van de Vossenberg, J.L., Driessens, A.J., and Konings, W.N. (1998). The essence of being extremophilic: the role of the unique archaeal membrane lipids. *Extremophiles* **2**, 163–170.
- Van Etten, J.L., Burbank, D.E., Xia, Y., and Meints, R.H. (1983). Growth cycle of a virus, PBCV-1, that infects Chlorella-like algae. *Virology* **126**, 117–125.
- Veesler, D., Ng, T.S., Sendamarai, A.K., Eilers, B.J., Lawrence, C.M., Lok, S.M., Young, M.J., Johnson, J.E., and Fu, C.Y. (2013). Atomic structure of the 75 MDa extremophile *Sulfolobus* turreted icosahedral virus determined by cryoEM and X-ray crystallography. *Proc. Natl. Acad. Sci. U S A.* **110**, 5504–5509.
- Wagner, C., Reddy, V., Asturias, F., Khoshouei, M., Johnson, J.E., Manrique, P., Munson-McGee, J., Baumeister, W., Lawrence, C.M., and Young, M.J. (2017). Isolation and characterization of *Metallosphaera* turreted icosahedral virus (MTIV), a founding member of a new family of archaeal viruses. *J. Virol.* **91**, <https://doi.org/10.1128/JVI.00925-17>.
- Wang, F., Cvirkaité-Krupovic, V., Kreutzberger, M.A.B., Su, Z., de Oliveira, G.A.P., Osinski, T., Sherman, N., DiMaio, F., Wall, J.S., Prangishvili, D., et al. (2019). An extensively glycosylated archaeal pilus survives extreme conditions. *Nat. Microbiol.* **4**, 1401–1410.
- Wirth, J.F., Snyder, J.C., Hochstein, R.A., Ortmann, A.C., Willits, D.A., Douglas, T., and Young, M.J. (2011). Development of a genetic system for the archaeal virus *Sulfolobus* turreted icosahedral virus (STIV). *Virology* **415**, 6–11.
- Wu, E., and Nemerow, G.R. (2004). Virus yoga: the role of flexibility in virus host cell recognition. *Trends Microbiol.* **12**, 162–169.
- Wuchter, C., Abbas, B., Coolen, M.J., Herfort, L., van Bleijswijk, J., Timmers, P., Strous, M., Teira, E., Herndl, G.J., Middelburg, J.J., et al. (2006). Archaeal nitrification in the ocean. *Proc. Natl. Acad. Sci. U S A.* **103**, 12317–12322.
- Zhilenkov, E.L., Popova, V.M., Popov, D.V., Zavalsky, L.Y., Svetoch, E.A., Stern, N.J., and Seal, B.S. (2006). The ability of flagellum-specific *Proteus vulgaris* bacteriophage PV22 to interact with *Campylobacter jejuni* flagella in culture. *Virol. J.* **3**, 50.

## STAR★METHODS

### KEY RESOURCES TABLE

REAGENT or RESOURCE	SOURCE	IDENTIFIER
Experimental Models: Cell Lines		
<i>Sulfolobus solfataricus</i> P222	(Ortmann et al., 2008)	
Bacterial and Viral Strains		
STIV1	(Rice et al., 2004)	
<i>E. coli</i> BL-21(DE3) pRIL	Agilent	Catalog #230245
Plasmids		
pEXP14-C381	This paper	
Deposited Data		
Coordinates of C381	This paper	PDB: 4IND
Coordinates of STIV1	(Veesler et al., 2013)	PDB: 3J31
Cryo-EM map of STIV1 bound to Sulfolobus	This paper	EMDB: EMD-20477
Cryo-EM map of STIV1 with Petals	(Rice et al., 2004)	EMDB: EMD-20618
Software and Algorithms		
HKL-2000	(Otwinowski and Minor, 1997)	RRID:SCR_015547 <a href="http://www.hkl-xray.com/hkl-2000">http://www.hkl-xray.com/hkl-2000</a>
Phenix	(Adams et al., 2010, 2013)	RRID:SCR_014224 <a href="https://www.phenix-online.org/">https://www.phenix-online.org/</a>
Coot	(Emsley and Cowtan, 2004)	RRID:SCR_014222 <a href="http://www2.mrc-lmb.cam.ac.uk/personal/pemsley/coot/">http://www2.mrc-lmb.cam.ac.uk/personal/pemsley/coot/</a>
Molprobity	(Davis et al., 2004, 2007)	RRID:SCR_003527 <a href="http://molprobity.biochem.duke.edu">http://molprobity.biochem.duke.edu</a>
UCSF Chimera	(Pettersen et al., 2004)	RRID:SCR_004097 <a href="http://plato.cgl.ucsf.edu/chimera/">http://plato.cgl.ucsf.edu/chimera/</a>
SerialEM	(Mastronarde, 2005)	RRID:SCR_017293 <a href="http://bio3d.colorado.edu/SerialEM/">http://bio3d.colorado.edu/SerialEM/</a>
IMOD	(Kremer et al., 1996)	RRID:SCR_003297 <a href="http://bio3d.colorado.edu/imod">http://bio3d.colorado.edu/imod</a>
PEET	(Heumann et al., 2011; Nicastro et al., 2006)	<a href="http://bio3d.colorado.edu/PEET/">http://bio3d.colorado.edu/PEET/</a>
RAVE	(Jones, 1992; Kleywegt and Read, 1997)	<a href="http://xray.bmc.uu.se/usf/rave.html">http://xray.bmc.uu.se/usf/rave.html</a>

### LEAD CONTACT AND MATERIALS AVAILABILITY

Further information and requests for resources and reagents should be directed to and will be fulfilled by the Lead Contact, Martin Lawrence ([lawrence@montana.edu](mailto:lawrence@montana.edu)).

### EXPERIMENTAL MODEL AND SUBJECT DETAILS

The archaeal cell and viral strains used in this study are listed in the [Key Resources Table](#).

### METHOD DETAILS

#### Quantification of Viral Attachment

*Sulfolobus solfataricus* strain P222 (available upon request, [myoung@montana.edu](mailto:myoung@montana.edu)) was grown to early log phase at 80°C and pH 2.5 as previously described (Ortmann et al., 2008). STIV was added to cells at a viral genome to cell ratio of 2 in a 500 µl microfuge tube. The virus and cells were incubated at 80°C with cells for times ranging from 0 – 40 minutes. Cells were then separated from unbound virus by three rounds of pelleting the cells at 5,000 × g for 5 minutes, discarding unbound virus in the supernatant, and resuspending the cells in media. After the final resuspension, cells were cultured for 24 hours, which represents one cycle of viral

replication. To estimate adsorption rate, the adsorption rate constant  $k$  was calculated using  $k = 2.3/Bt \times \log_{10} (P_{max}/P_t)$ , where  $B$  = concentration of host cells as number of cells per milliliter,  $P_{max}$  = average maximum viral yield obtained, and  $P_t$  = viral yield at time  $t$  (Puck et al., 1951). Absorption rate constants for other viruses presented in Table S1 were obtained from the following references: SMV1 (Uldahl et al., 2016), SSV9 (Bautista et al., 2015), and SIRV2 (Quemin et al., 2013). Bacteriophages: T1-T4 (Puck et al., 1951),  $\phi 6$  (Olkkinen and Bamford, 1989), and PV22 (Zhilenkov et al., 2006). Halophilic archaeal viruses SH1, HHTV1 His1, and His2 (Svirskaitė et al., 2016). Algal virus PBCV-1 (Van Etten et al., 1983).

### Phylogenetic Tree and Identification of Conserved Residues in C381

Using the C381 sequence of STIV-1 or the analogous region of B631 from STIV-2, Blast searches were performed on a collection of metagenomic sequence data from Yellowstone National Park thermal features (Bolduc et al., 2015), cellular isolates and publicly available sequences using both tBLASTn and psi-blast programs (Altschul et al., 1997; Camacho et al., 2009). Extracted protein sequences were aligned with ClustalW (Blosum Matrix, gap open 15, gap extend 1) and realigned with MUSCLE (default settings) (Edgar, 2004; Larkin et al., 2007). Sequences greater than 75% of full length C381 were then used to build a phylogenetic tree with MEGA X using a Maximum Likelihood method and JTT matrix-based model over 2000 bootstrap iterations (Kumar et al., 2018). The sequence alignment used to construct the phylogenetic tree is shown in supplemental data (Data S1). All sequences belonging to the STIV-1 clade, including those less than 75% of full length, were subsequently realigned with ClustalW and used to identify strictly conserved residues (Data S2). The accession numbers for all sequences are indicated in Figure S3, Data S1, and Data S2.

### Expression, Purification and Crystallization of C381

C381 was cloned into pDEST14 (Invitrogen) as previously described (Kraft et al., 2004; Schlenker et al., 2012), yielding the expression vector pEXP14-C381. Internal forward and reverse primers for nested PCR were TTGAAAGGAGATAGAACCATGAGTGGTACTA CATTGGG and GTGATGGTGATGGCTAGTTCTCCCGCTATT, respectively. External primers were reported previously (Menon et al., 2010), as was the protein expression protocol with the following modifications (Lintner et al., 2011). Lysis buffer was 20 mM Tris, 400 mM NaCl, 10 mM imidazole (pH 8.0), the Ni-NTA wash buffer was 20 mM Tris, 400 mM NaCl, 20 mM imidazole (pH 8.0), Ni-NTA elution buffer was 10 mM Tris (pH 8.0), 50 mM NaCl and 200 mM imidazole, and size exclusion chromatography buffer was 10 mM Tris (pH 8.0), and 50 mM NaCl. Purified C381 was concentrated to 10 mg/ml using 30 kDa MWCO Amicon Ultra centrifugal filters. The protein was crystallized by sitting drop vapour-diffusion at 18°C using 2 µl of C381 and 2 µl of well solution (30-40% PEG 600, and 0.1 M sodium phosphate, dibasic/citric acid pH 4.2). Once initial crystals were obtained micro-seeding was employed at times to speed crystallization and increase the number of crystals.

### C381 Crystallographic Structure Determination

The crystal structure of C381 was determined by Single Wavelength Anomalous Diffraction (SAD). The native and single-wavelength anomalous diffraction data sets at the Se-K edge were collected at the Stanford Synchrotron Radiation Laboratory (beamlines 12-2 and 9-2 respectively). Data were processed in space group P1 with HKL2000 (Otwinowski and Minor, 1997). Crystal parameters and statistics on data quality are presented in Table 1. The AutoSol module of PHENIX (Adams et al., 2010) was used to identify the selenium atom substructure in the 2 subunits present in the asymmetric unit/unit cell, to calculate initial phases, and to build an initial model. Phases were then transferred to the higher resolution native data set. The structural modeling was then completed with Coot (Emsley and Cowtan, 2004) and refined with the phenix.refine module of PHENIX (1). Model validation was done with Molprobity (Davis et al., 2007). Statistics on refinement and model quality are presented in Table 2. The model has been deposited in the Protein Data Bank (PDB: 4IND). Figures were generated with Chimera (Pettersen et al., 2004). Structural similarities between C381 and other proteins in the PDB were identified with the DALI server (Holm and Rosenstrom, 2010).

### Negative Stain Electron Microscopy

1 ml *S. solfataricus* P222 cells at approximately  $5 \times 10^8$  cells/ml was combined with 100 µl of 1.88 mg/ml virus and incubated for 20 minutes at 80 °C. Unbound virus was removed by centrifugation as described above. Final resuspension was in 15 µl of 5 mM Citrate at pH 2.5. Cells with bound virus were stained with 2% uranyl acetate on carbon coated grids prior to transmission electron microscopy (TEM) using a LEO 912AB with 2Kx2K CCD camera.

### Cryo-Electron Tomography

Cells with bound virus in 5 mM Citrate were obtained as described above and frozen on Quantifoil R2/1 holey carbon grids (200 mesh copper) in liquid propane/ethane using a Vitrobot Mark III (FEI, Hillsboro, OR). Tilt series were taken using a Titan Krios (FEI, Hillsboro, OR) operated at 300 kV and equipped with a Volta phase plate (Danev and Baumeister, 2017; Khoshouei et al., 2017), a Quantum post-column energy filter (Gatan, Pleasanton, CA), and a Summit K2 camera (Gatan, Pleasanton, CA) operated in electron counting mode. Tilt-series images were collected using SerialEM (Mastronarde, 2005). Individual frames of images acquired with the K2 camera were aligned in Digital Micrograph (Gatan, Pleasanton, CA). Acquisition parameters were: magnification 35,700 X; tilt range +/-60°; tilt increment 2°; total dose ~60 e<sup>-</sup>/Å<sup>2</sup>; pixel size 0.14 nm/px; defocus with phase plate -0.25 µm. The Volta phase plate was operated as previously described (Danev et al., 2014; Fukuda et al., 2015).

Tomograms were reconstructed using IMOD 4.7 (Kremer et al., 1996). Contrast transfer function (CTF) corrections were not performed. Gold nanoparticles were used as fiducial markers for alignment of tilt-series projection images. Local alignment solutions were used for rotation, magnification, and tilt angle, while a global solution was employed for distortion. Gold particles were erased from the final aligned stack. Images were binned 2x, radially filtered with a cutoff of 0.4 and falloff of 0.05, and run through 10 SIRT iterations. Alternatively, images were binned 2x but left unfiltered and weighted backprojection used for the reconstruction. These unfiltered weighted back projections were used for subtomographic and icosahedral averaging of STIV.

### Subvolume Alignment and Averaging for STIV

Virus particles were aligned from the filtered tomograms using Particle Estimation for Electron Tomography (PEET) (Heumann et al., 2011; Nicastro et al., 2006), with the 3.9 Å structure previously determined by single-particle analysis used as an initial reference (Veesler et al., 2013). The motive list was then used to align and extract virion sub-volumes from the unfiltered tomograms. Excised particles were translated using MAPMAN in the RAVE averaging package (Jones, 1992; Kleywegt and Read, 1997) such that the center of the volume/particle was at the origin. Particles were then subjected to 60-fold averaging with strict icosahedral symmetry using AVE (Jones, 1992; Kleywegt and Read, 1997). Finally, the density for 6 icosahedrally averaged particles were summed within Chimera using VOP (Pettersen et al., 2004).

### Subvolume Alignment and Averaging for Pili

Model points were manually placed along host pili with additional points then being added every 5 nm with addModPts. This resulted in 1774 sub-volumes that were then aligned and averaged with PEET (Heumann et al., 2011; Nicastro et al., 2006). Particle model points were used to specify the Y-axis and random axial rotations were used for the initial motive list. For a reference, a cylindrical volume with a diameter of 6 nm was generated with the Shape command of Chimera (Pettersen et al., 2004). To prevent misalignment near viral particles, density associated with the capsid was set to zero.

### Subvolume Alignment and Averaging of the Turret/Pilus Interaction

Viral turrets located near host pili were chosen as candidates for pilus/turret junction averaging. Identification of these sites was further aided by using the clonevolume program of PEET (Heumann et al., 2011; Nicastro et al., 2006) to place averaged virus density into the tomogram. Model points were placed at the center of each virion and at the center of each candidate turret. The stalkInit program was then used to calculate the initial motive list and rotation axis. The entire capsid was utilized for alignment of the chosen turret along the y-axis with PEET (Heumann et al., 2011; Nicastro et al., 2006). At this stage Theta and Psi were determined, and due to the five-fold symmetry of the turret, only 5 possible solutions remained for Phi.

To build an initial reference, three interactions were chosen with long straight sections of pilus traversing them. These were skewed into a common orientation using the appropriate rotation matrixes and the average command of AVE from Uppsala Software (Jones, 1992; Kleywegt and Read, 1997). After generating the initial reference, candidate turrets were rotated about the y-axes in 72° increments (exploiting the 5-fold symmetry of the turret) to search for correct alignment to the reference. A spherical mask was used to score only density near the turret pilus junction. Background noise levels were determined using 30 dummy particles with no pilus.

### Fitting the Atomic Structure of STIV into the Subvolume Average

Subvolume averages were determined to be larger than the atomic model necessitating scale correction. Using Alterheader from IMOD, a series of resized capsids were generated in 0.01 Å increments by modifying the pixel size. These resized capsids were then resampled onto the original volume using Chimera (Pettersen et al., 2004). Cross correlation values were calculated between each resized sub-tomogram and the 4.5 Å single particle reconstruction using PEET with search angles and distance set to zero (Heumann et al., 2011; Nicastro et al., 2006). Alternatively, Fourier shell correlations were calculated using algorithms from EMAN2 and Imagic implemented in the PDBe Fourier Shell Correlation server (Abbott et al., 2018).

### QUANTIFICATION AND STATISTICAL ANALYSIS

Tables 1 and 2 contain statistics for the crystal structure determination. The analysis and software used are described in detail within the Method Details section.

### DATA AND CODE AVAILABILITY

The metagenomic sequences matching C381 are available in GenBank with accession numbers GenBank: MN091862 through GenBank: MN091923. The C381 sequences from NG5 and Y14 are available in GenBank (accession numbers GenBank: CP020360.1 and GenBank: CP013695.1 respectively). The accession number for the crystallographic structure of C381 reported in this paper is PDB: 4IND. The accession number for the averaged tomographic model for the STIV-Pili interactions (Figure 5K) reported in this paper is EMDB: EMD-20477. No new code was generated.